H_2O Megamasers: Measuring the Mass of The Black Hole in the Active Nucleus of Markarian 1210

Stephen S. Clouse

A senior thesis submitted to the faculty of
Brigham Young University
in partial fulfillment of the requirements for the degree of

Bachelor of Science

Victor Migenes, Advisor

Department of Physics and Astronomy

Brigham Young University

August 2012

ABSTRACT

H_2O Megamasers: Measuring the Mass of The
Black Hole in the Active Nucleus of Markarian 1210

Stephen S. Clouse
Department of Physics and Astronomy
Bachelor of Science

In this study we present a map of the water maser emission from the nucleus of the Seyfert 2 galaxy Mrk 1210, as observed with the Very Long Baseline Array. We detect red-shifted and blue-shifted masers but detect none at the systemic recession velocity of the galaxy. Observations by the Green Bank Telescope (GBT) show a spectral profile of the megamasers that is somewhat unlike the characteristic triple-peaked profiles of classic water megamasers in AGN accretion disks. However, our map shows that the masers are aligned roughly perpendicular to extended radio continuum structures in the nucleus, suggesting the masers come from the accretion disk. We find that we can fit the megamaser distribution with a flat, inclined disk, with two of the maser loci falling near the midline of the disk and a third coming from an azimuthal angle of 47 degrees on the near side of the disk. We also find them all to have accelerations less than 0.25 km s^{-1} yr^{-1}, which is consistent with the flat disk model. With this scenario, we can estimate the mass of the central black hole to be approximately 1.3×10^7 $M_\odot$.

Keywords: accretion, accretion disks— galaxies: individual (Markarian 1210)—galaxies: nuclei—masers

ACKNOWLEDGMENTS

I would first like to acknowledge my wife for her patience and support during my undergraduate education and research. I would also like to thank my advisors, Dr. Victor Migenes at Brigham Young University and Dr. James Braatz at the National Radio Astronomy Observatory. Their priceless examples have provided an outline for me as a researcher. The largest influence on my future career in Astrophysics comes from their diligence and care in helping me be successful. I would also like to thank Dr. Cheng-Yu Kuo for the many times he poked his head in my office door to make sure that I was successfully understanding the AIPS reduction process. Thank you all for all your help, I could not have done any of it without you.

Contents

List of Figures

Chapter 1

Introduction

1.1 Motivation

Some of the most important research that is being done in physics today concerns understanding the cosmological universe. The Megamaser Cosmology Project (MCP) is a collaboration of many scientists from around the world whose work is centered around increasing our understanding of this topic. Using highly accurate measurements of the active centers of galaxies, they have determined a way to probe the universe and discover many of the universe's cosmological properties.

Edwin Hubble's discovery of an expanding universe may be the most important discovery that has been made in the field of cosmology. The Hubble Constant, H_0, relates the velocity of a galaxy to its distance from the earth. Accurate measurements of H_0 are important to understanding the way the universe has evolved since the big bang and will continue to evolve in the future. Many methods have been developed for measuring the Hubble constant, each giving various values and varying uncertainties. The goal of the MCP is to measure H_0 directly within 3% accuracy (Braatz Accessed February 2, 2012). By measuring H_0 to such high accuracy, scientists will better understand the expansion of the universe and its evolution.

The method developed by the MCP uses precise measurements of circumnuclear H_2O megamasers in the accretion disks of Active Galactic Nuclei (AGN) to make direct calculations of the distance to many galaxies. In addition to cosmological calculations, an accurate central black hole mass can be derived from the data. Obtaining the central black hole mass for a large sample of galaxies is important for determining the M-σ relation which is a correlation that has been found between the masses of central black holes (M) and the velocity dispersion (σ) of stars found within their central bulge (See Fig. 3.10). The reason for this correlation has not yet been discovered, but many believe it may rise from the fact that the evolution of the bulge is linked to the evolution of the central black hole (See (Ferrarese & Merritt 2000)). Finding this relationship for more galaxies may teach us more about galactic evolution and enable us to determine why this correlation exists.

The black hole mass measurement is significant to the M-σ relation due to the accuracy of the techniques used. Because the megamasers lie within the inner most parsec (pc) of the disk, their orbital motions are dominated entirely by the mass of the black hole. Other stellar methods of measuring the central black hole mass use stars in nuclear star clusters. These are less accurate because the stars have an orbital radius of ~ 50 pc, thus introducing the possibility that other stars may perturb their gravitational motions. Currently the MCP has accurately measured the mass for supermassive black holes of 8 galaxies.

For a more detailed overview of the theoretical and observational goals of the MCP, see (Reid et al. 2009). For this project we will present the methods and results of observations of H_2O megamasers in the cirumnuclear disk of Mrk 1210.

1.2 Maser Science-H_2O Megamasers

In 1953 Charles Townes invented a device called the maser (microwave amplification by stimulated emission of radiation). His design techniques were based on theory which was provided by Nicolay

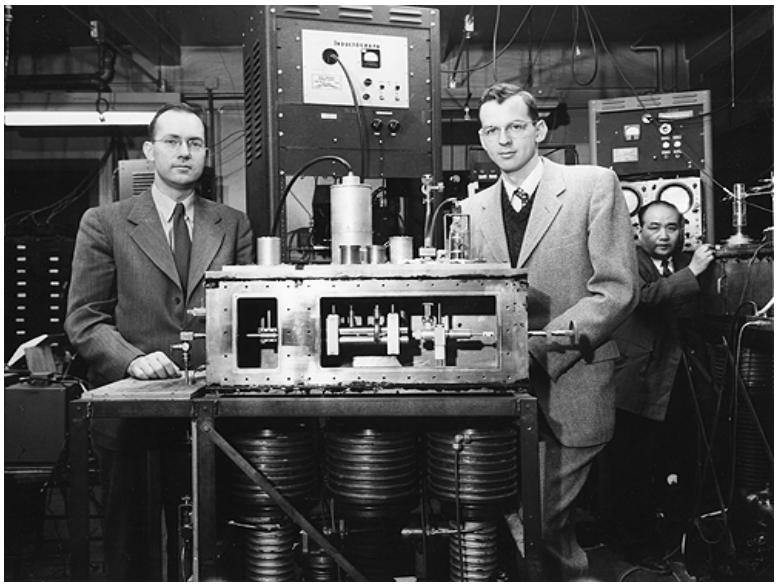

Figure 1.1 Charles Townes (left) and James P. Gordon display their maser, a device that amplifies microwaves. They discovered that when molecules of ammonia became excited, they could be stimulated to emit microwaves (Advameg Accessed February 29, 2012).

Basov and Aleksandr Prokhorov in 1952 (The Nobel Foundation, Accessed January 23, 2012). Townes discovered that if he excited molecules of ammonium, they would emit amplified coherent microwaves. See Fig. 1.1 for a picture of Townes next to the device. Their work explained many of the facets of stimulated emission. These ideas have become important in many fields of science and technology, including the field of astronomy with the astrophysical maser.

As stated in its name, the maser functions through a stimulated emission process, as does the laser (light amplification by stimulated emission of radiation). The difference between them is the wavelength at which they emit. Lasers emit coherent radiation at optical wavelengths caused by the transitions of electrons from energy levels in the outer orbitals of an atom, while masers emit radiation in the microwave and radio wavelengths caused by rotational transitions in molecules.

In order for stimulated emission in a maser to occur, several environmental conditions must be met. First, the gas must have a relatively high density. In masers, the particle density is typically on the order of $10^6 - 10^9$ particles per cubic centimeter. Secondly, there must be a pumping

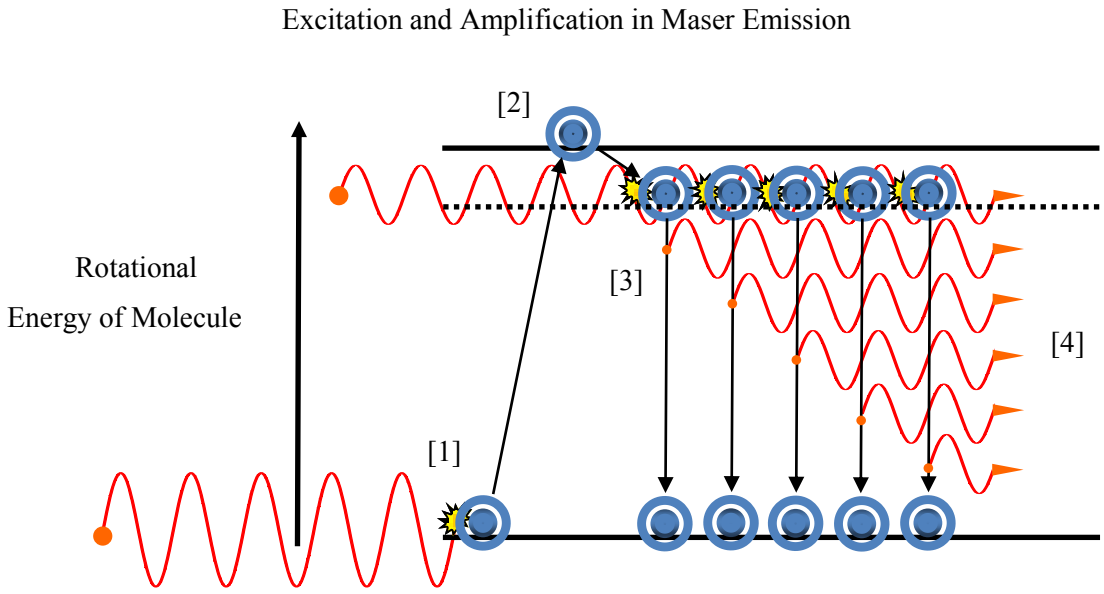

Figure 1.2 This is a diagram of the stimulated emission process. First the molecule is brought into an excited state by an incoming photon. The molecule then decays to a long lived metastable state. Third, an incoming photon de-excites the molecule causing each to emit radiation of the same frequency (energy). A beam of coherent amplified radiation is then emitted from the molecular gas.

mechanism. Pumping occurs when exterior energy, usually from a continuum emission source, causes the molecules in a molecular gas to become excited (brought to a higher energy level). After being excited, the molecules will then quickly decay down to a longer lived, metastable energy state. Additionally, a population inversion must take place. A population inversion occurs when the majority of the molecules in the gas are brought into this metastable state. When these conditions are met, the environment is in a state where "masing" can occur. See Fig. 1.2 for a complete diagram of the stimulated emission process.

After a population inversion, masing occurs by interactions with a photon from a continuum source, whose energy corresponds to the energy difference between the molecule's metastable and ground state. The interaction of the photon with the molecule causes its rotational energy to transition to the ground level. A photon of the same frequency and phase will then be emitted. With two photons of the same energy and phase leaving the molecule they will constructively interfere with each other, causing amplification by stimulated emission.

There are two different types of amplification inside a maser environment, depending on the photon saturation of the molecules. If the molecular cloud is unsaturated, the external pumping mechanism can repopulate the molecules faster than stimulated emission can depopulate them. If the cloud is saturated, the external pumping mechanism cannot populate them at this same rate. The equation of radiative transfer for an unsaturated cloud of gas is

$$\frac{dI_\nu}{ds} = \kappa_\nu I_\nu \Rightarrow I_\nu = I_0 e^{\tau_\nu}, \tag{1.1}$$

where

$$\tau_\nu = \kappa_\nu \rho s. \tag{1.2}$$

In these equations I_ν is the frequency dependent intensity, κ_ν is the opacity of the gas, I_0 is the background intensity at the given frequency, τ is the optical depth of the gas, ρ is the density of

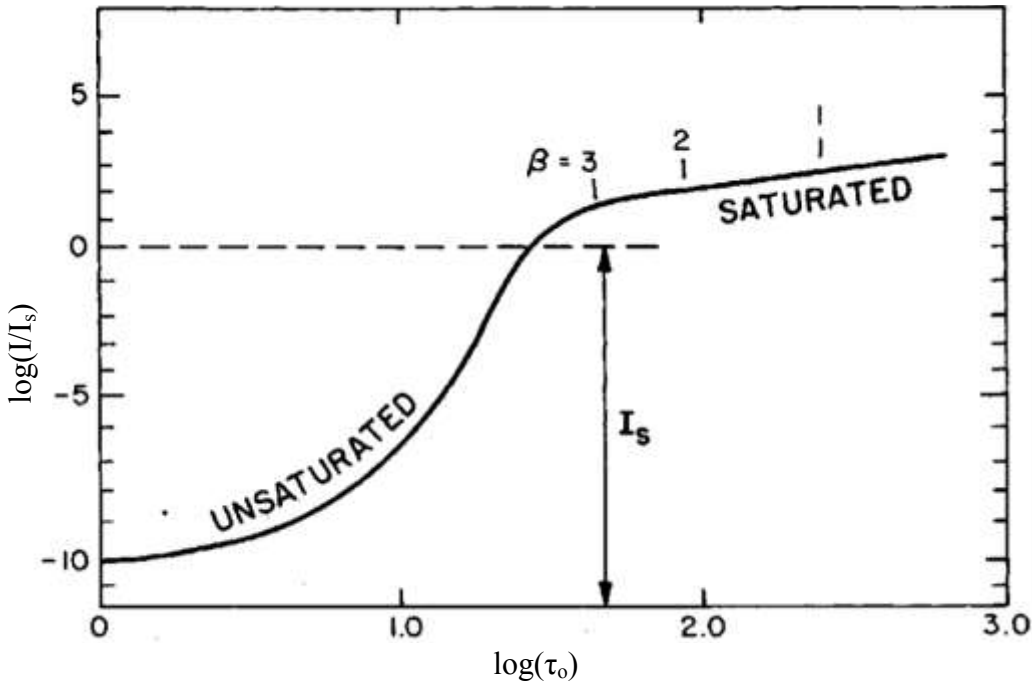

Figure 1.3 This graph depicts the differences in intensity vs optical depth in unsaturated vs. saturated masers. As is seen, unsaturated masers have an exponential growth in intensity as you increase the optical depth while saturated masers do not.

the gas, and s is the thickness of the gas. Similarly for a saturated molecular cloud, the equation is

$$\frac{dI_\nu}{ds} = \kappa_\nu I_s \Rightarrow I_\nu = I_0 + \tau_\nu I_s, \tag{1.3}$$

where I_s scales how the intensity increases linearly with cloud thickness. You can see that for an unsaturated molecular cloud, as you increase the path length of gas through which the photons transmit you have an exponential increase in the observed intensity of the maser source. While for a saturated cloud, the increase is linear with path length. See Fig. 1.3 for relationship between optical depth and intensity.

Certain environments in the interstellar medium (ISM) provide the proper conditions for masers. In star forming regions there are often large molecular clouds with the right densities and temperatures for masing to occur. The central black holes of active galactic nuclei (AGN) provide energy

that is needed in order to pump masers found within their accretion disks. Supernova remnants eject material into space creating large energetic clouds. In some galaxy mergers, huge clouds of gas smash into each other creating dense molecular environments which are perfect nurseries for masers. These examples illustrate a small number of the many ideal environments for stimulated emission. Since astrophysical masers have small bandwidths, are point-like, and have large amplified intensities; they are ideal for probing the proper motions and physical conditions of various regions in the universe.

Observations of the majority extragalactic masers show that their intensities are not typical of masers observed within our own galaxy. These ultra-luminous masers are called megamasers and are about one million times more luminous than galactic masers. If a region contains a large volume of gas, this can lead to larger path-lengths along the line of site, and thus, larger amplification in the maser. The reason megamasers have not yet been discovered within our own galaxy is unknown. Due to these high intensities, megamasers are extremely useful. They enable us to see the dynamics of galaxies that are extremely far away, thus allowing us to learn about galactic evolution and about the expansion of the universe as a whole.

As mentioned previously, astrophysical masers are found in many different environments. They also come in many molecular forms. Masers are found in large varieties while megamasers have only been discovered in water (H_2O), formaldehyde (H_2CO), and methine (CH). Each molecular species has its own properties and specific environments. For a brief overview of many of the possible maser environments with their molecular types, see (Buizer 2007). Water megamasers, which are the focus of this paper, are primarily found in the accretion disks of AGN (Lo 2005).

1.3 Description of Active Galactic Nucleus (AGN) Environment

Active galaxies are identified by a unique set of characteristics that distinguish them from "normal" galaxies. As is stated in (Ryden & Petersen 2010), these characteristic are as follows:

- Active Galaxies produce large amounts of nonstellar emission, some of it nonthermal in origin, arising from energetic and violent processes. Active galaxies produce more radio and x-ray emission than you'd expect if all their light came from the photospheres of stars.
- Active galaxies have much of their light concentrated in a small, central region know as an active galactic nucleus, or AGN.
- Light from AGNs is variable on short timescales at virtually all wavelengths. The timescale for significant variability is dependent on both luminosity and wavelength.
- Some active galactic nuclei have jets that are detectable at x-ray, visible, and radio wavelengths. The jets contain ionized gas flowing outward at relativistic speeds.
- The ultraviolet, visible, and infrared spectra of AGNs are dominated by strong emission lines.

These characteristics indicate that the activity in active galaxies directly correlates with the accretion of matter onto a central supermassive black hole. Additionally, for the galaxy to be classified as "active," the accretion rate must be high enough to cause the AGN's luminosity to be higher than the stars in the galaxy.

While many galaxies have been classified as "active" there are also many subclassifications for AGN. An overview of each is given in Fig. 1.4 and Table 1.1. According to the unified model of active galactic nuclei, type 1 AGN's are seen as having a face on nuclear disk and have both narrow and broad emission lines, while type 2 AGN's are seen edge-on and have only narrow emission lines, which are commonly believed to be intrinsically the same as type 1 AGN's. (Wu et al. 2011)

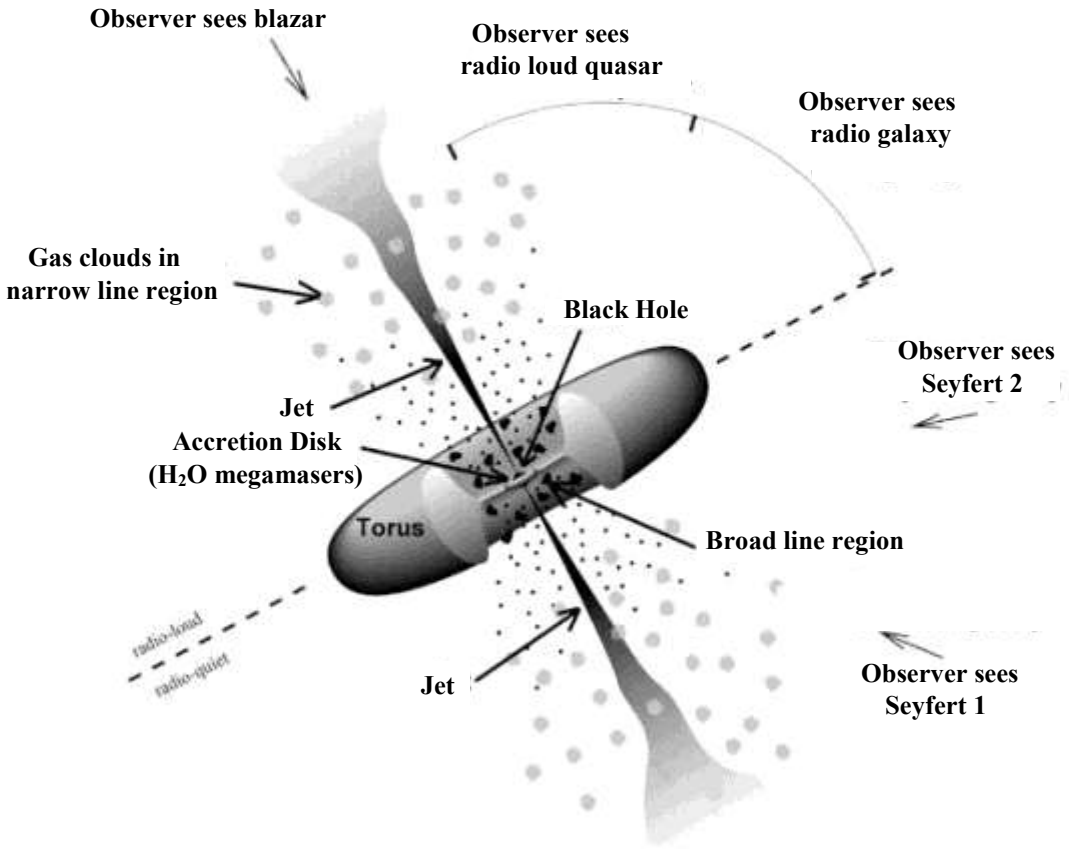

Figure 1.4 A modified version of the Unified Model of AGN (CalTech Accessed February 29, 2012). As can be seen in the figure, AGN classification is dependent on the observed angle of the black hole. The largest column densities in the accretion disk occur when observed from edge-on or nearly edge-on. This is true for Seyfert 2 galaxies.

Table 1.1 Characteristics of AGN Under the Unified Model

Galaxy Type	Active Nuclei	Narrow Emission	Broad Emission	X-Rays	Excess UV	Excess Far-IR	Strong Radio	Jets	Variable	Radio Loud
Normal	no	weak	none	weak	none	none	none	none	no	no
Starburst	no	yes	no	some	no	yes	some	no	no	no
Seyfert I	yes	yes	yes	some	some	yes	few	no	yes	no
Seyfert II	yes	yes	no	some	some	yes	few	yes	yes	no
Quasar	yes	yes	yes	some	yes	yes	some	some	yes	10%
Blazar	yes	no	some	yes	yes	no	yes	yes	yes	yes
BL Lac	yes	no	none/faint	yes	yes	no	yes	yes	yes	yes
Radio Galaxy	yes	some	some	some	some	yes	yes	yes	yes	yes

Note. – This table shows the different types of AGN with their characteristics. (Wikipedia Accessed March 29, 2012).

In other words, unified models suggest that the classification of AGN is dependent on the viewing angle of the accretion disk as is shown in the figure. As was mentioned in Section 1.2, the amount of amplification in a maser is dependent on the path length of the emitting molecular cloud. In order to get the largest path length possible, the molecular accretion disk of the AGN must be viewed from nearly edge-on. For this reason, all H_2O megamaser disks have been found within Seyfert 2 galaxies.

AGN accretion disks provide the perfect environments for masing to take place. The central AGN provides infrared radiation necessary for pumping to occur. Dust found closer to the central black hole shields the masers from harmful ultra violet radiation which will cause photodissociation in the H_2O molecules. The accretion disk also has the densities and temperatures needed to create masers as mentioned in section 1.2.

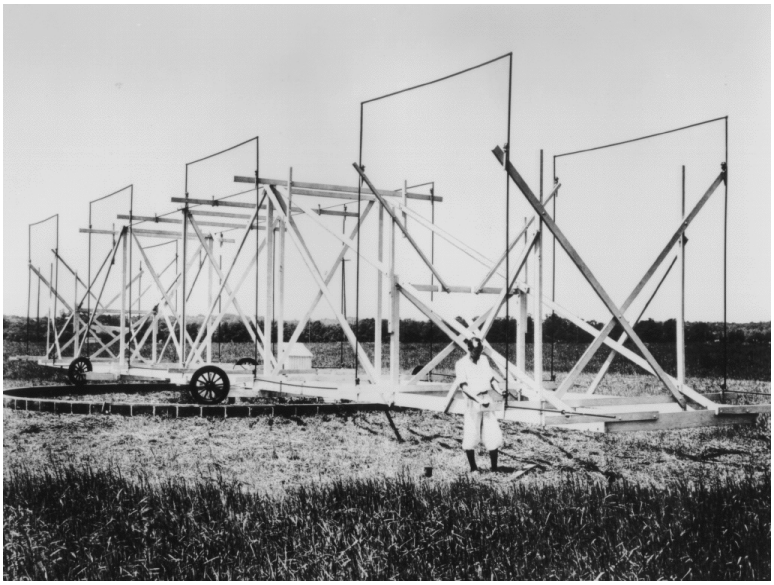

Figure 1.5 This photograph of Jansky and his radio receiver was taken in 1933. The antenna array turned a full circle every 20 minutes on Model T wheels (Sullivan 1978).

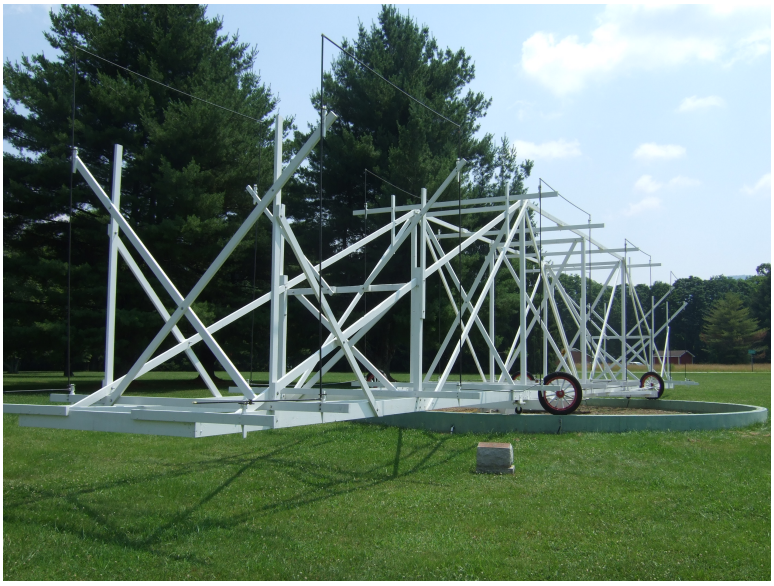

Figure 1.6 This is a rejuvenated version of the Jansky Array owned by the National Radio Astronomy Observatory (NRAO) found in Green Bank, WV. Photograph supplied by the Author.

1.4 Radio Astronomy History Important Figures

The first astrophysical object detected at radio wavelengths was by Karl Guthe Janksy in 1932. He was hired by Bell Telephone Laboratories to investigate the nature of the "atmospherics," or statics affecting the telephone company's shortwave radio telephone circuits. In order to do this, Jansky built a special receiver for detecting these waves. See Fig. 1.5. After carefully studying the first few months of records, it was clear that there were three main types of static. Jansky describe them as follows: "From the data obtained it is found that three distinct groups of static are recorded. The first group is composed of the static received from local thunderstorms and storm centers. Static in this group is nearly always of the crash type. It is very intermittent, but the crashes often have very high peak voltages. The second group is composed of very steady weak static coming probably by Heaviside layer (ionosphere) refractions from thunderstorms some distance away. The third group is composed of a very steady hiss type static the origin of which is not yet known (Sullivan 1978)." As his observations continued he noticed that it seemed the hiss was coming from the sun. This was very misleading because in the wintertime the sun is very near the constellation Sagittarius, the true source of the static. As time went on Jansky realized he had made a very important discovery. The hiss was actually coming from the center of the Milky Way galaxy. A replication of Jansky's array is owned by the NRAO and is shown in Fig.1.6.

Although Jansky's discovery was important, it was not initially accepted by the scientific community because he was an electrical engineer and not an astronomer. It wasn't until five years later that Grote Reber, an amateur astronomer, decided to see if he could also detect radio emissions from the celestial sphere. Grote Reber built the first radio dish designed solely for astronomical observations in 1937 shown in Fig. 1.7 and Fig. 1.8. Reber mapped out the milky way galaxy at radio wavelengths. Grote Reber's expertise in radio astronomy built a foundation for what radio astronomy is now. He oversaw many astronomical projects for radio astronomy up until his death in 2002 (NRAO Accessed March 7, 2012).

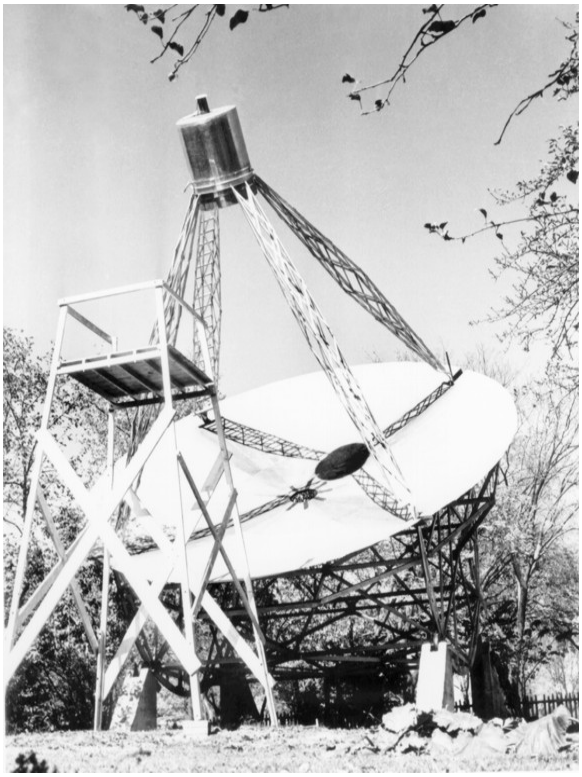

Figure 1.7 This is a photograph of Reber's Radio dish in 1937. The parabolic mirror, made of sheet metal 31.4 feet in diameter, focuses radio waves to a point 20 feet above the dish (NRAO Accessed March 7, 2012).

Figure 1.8 Reber's telescope now sits at the NRAO in Green Bank, WV. Photograph supplied by the Author.

1.5 Very Long Baseline Interferometry (VLBI)

Very Long Baseline Interferometry (VLBI) is the process of combining signals from multiple separated antennas. VLBI techniques are useful due to their ability to resolve small angular scales, especially at radio wavelengths. The resolution limit is given by the Rayleigh criterion which states that

$$\theta_{min} = 1.22\frac{\lambda}{D}. \tag{1.4}$$

Where θ_{min} is the minimum angular resolution, λ is the wavelength, and D is the diameter of your telescope. Since radio waves have such long wavelengths, you would need to build a radio dish with an extremely large diameter in order to have high angular resolution. Current engineering and monetary constraints make this impossible. For example, the Hubble Space Telescope, with an aperture size of 2.4 meters, can resolve objects as small as 0.082 asec. In order to get the same resolution at a frequency of 22 Ghz, you would need to build a dish with a diameter of about 60 kilometers, which is obviously impossible. This resolution can be obtained feasibly using interferometry. For this project, we used the Very Long Baseline Array (VLBA) (See Fig. 1.9). The VLBA has ten antennas, containing a baseline of approximately 8000 km, giving it an incredible resolution of about 0.000429 asec at 22 Ghz. With a potential to resolve extremely small angular scales, radio astronomy has been driven to larger and larger arrays.

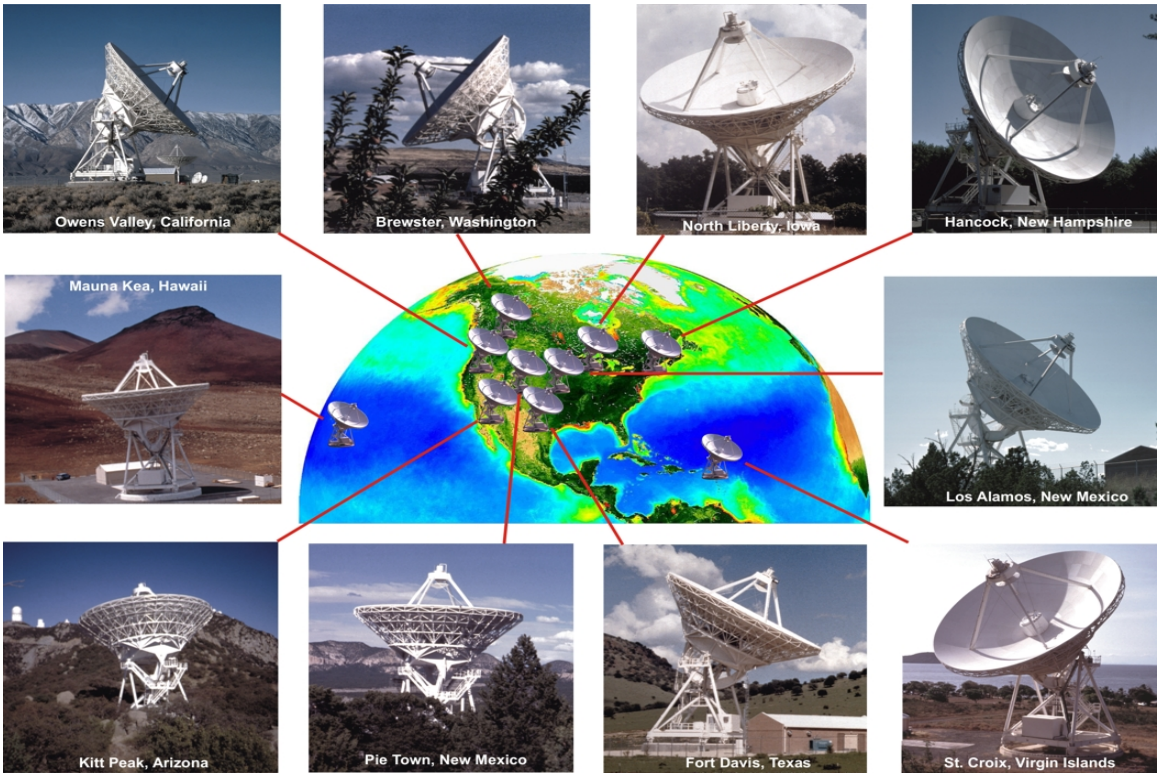

Figure 1.9 This shows the locations of the Very Long Baseline Array (VLBA) Antennas. With such large baselines, the VLBA can resolve small angular scales. Image credit (NRAO Accessed February 29, 2012).

Chapter 2

Methods

2.1 Cosmology with H_2O Megamasers

The MCP and its pilot programs have discovered masers in 58 galaxies, 40% of all known extragalactic water masers and have been discovered using instruments like the GBT and the Effelsburg telescope as outlined in (Braatz Accessed February 2, 2012). Many have since been mapped with instruments like the VLBA. By combining periodic spectral observations with the radio maps, many of these objects can be used to measure the distances to their host galaxies and determine the mass of the their central black holes.

After discovering extragalactic H_2O-megamaser emission, unique spectral features can help determine if its emission is coming from an accretion disk. See Fig. 2.1 for the classic H_2O-megamaser disk spectral profile of UGC 3789. As can be seen, the object has three distinct peaks. These peaks arise from different recession velocities in the disk. The central peak emission comes from masers that are often referred to as the systemic masers because their velocities correspond to the velocity of the galactic system. The highly blue-shifted and red-shifted features are approximately equally spaced from the recession velocity and correspond to megamasers found away

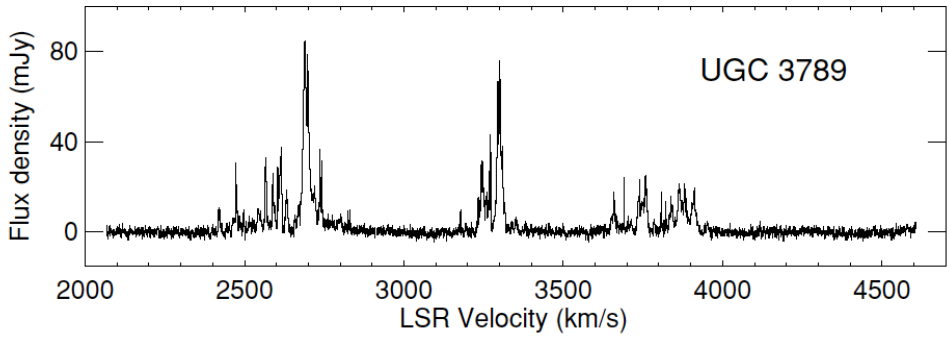

Figure 2.1 The spectral profile of UGC 3789 taken by the GBT. This is a classic megamaser disk profile. Spectra from (Braatz et al. 2010).

from the central black hole along a region of the disk called the midline. See Fig. 2.4 for a visual representation of the midline masers.

After it has been determined that the spectral emission is coming from a disk, VLBI measurements are taken to determine angular-distance measurements from each maser feature. Fig. 2.2 gives the corresponding map of UGC3789 with its position-velocity (P-V) plot. As can be seen, all the maser features are found within a flat, edge-on disk structure. The systemic masers being located at the center of the disk, with the red-shifted and blue-shifted maser features found along the midline. The P-V plot provides additional evidence that the masers are in a disk. As is shown in the plot, the maser velocities follow a Keplerian fit, with higher absolute velocities found closer the the central black hole, implying that the masers are located along the midline.

In addition to high-resolution maps, periodic spectral measurements of the source must be taken in order to calculate accurate accelerations for each maser feature. By fitting a Gaussian profile to each spectral feature, precise velocities are determined. By plotting these velocities with their corresponding observation time, accurate accelerations are calculated by fitting a line through the data and taking the time derivative of the fit. Fig. 2.3 shows the velocity of each maser feature plotted against observing time in UGC 3789. The slope of each linear fit in the plot

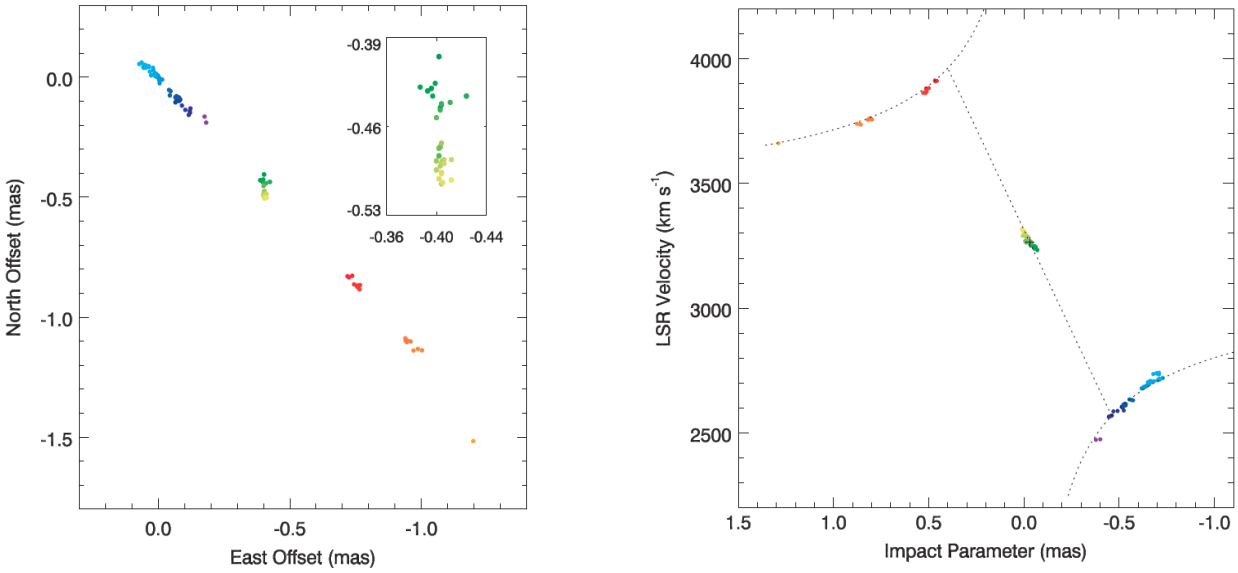

Figure 2.2 The VLBI map of UGC 3789 taken by the VLBA with the associated position-velocity (P-V) diagram. As can be seen, the velocities of the masers correspond to keplerian models, implying that the masers are found within a disk. Map and diagram provided by (Reid et al. 2009).

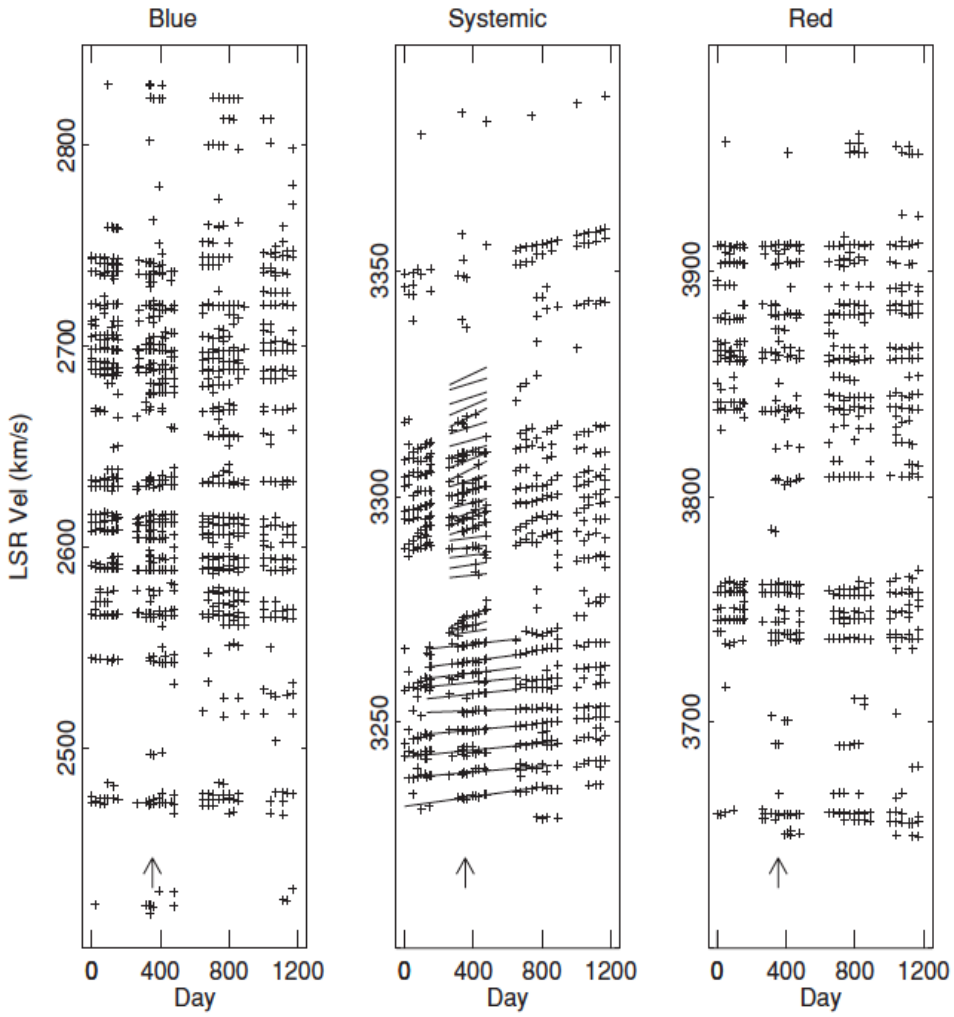

Figure 2.3 The acceleration measurement of the megamasers in UGC 3789 derived from the GBT spectra. As is seen, the systemic masers have high accelerations while the red and blue shifted masers have an acceleration of nearly zero. Image provided by (Braatz et al. 2010).

represents the acceleration of a given maser. The velocities and accelerations that were measured are the components projected along the line of site. As is expected, the systemic masers have large accelerations (large slope in the linear fits) while the red-shifted and blue-shifted masers having essentially no acceleration since all accelerations are directed towards the central black hole. With the accelerations projected along the line of sight this means that the systemic accelerations are true accelerations while the highly red-shifted and blue-shifted masers have accelerations that are perpendicular to the line of sight, giving zero acceleration.

The locations of the masers along the midline can be retrieved from the P-V diagram. As is shown in Fig. 2.2, the masers along the midline of the disk follow a Keplerian curve while the systemic masers follow a linear trend. Fig. 2.4 shows the implications of the P-V curves. A linear trend in the P-V diagram implies that the systemic masers are all the same distance from the central black hole, unlike the masers that fall along the midline. The midline masers velocities follow a Keplerian curve, with higher velocities found for masers near the central black hole. A linear fit can be applied to the velocities of the systemic features, as shown in Fig. 2.2. Since the linear fit associates masers that are at the same radius, the systemic features can be associated with one of the highly red or blue shifted masers that has the same orbital radius. Since the masers are at the same radius, we know that they have the same velocity and acceleration. The actual orbital acceleration is the measured acceleration of the systemic feature and the actual orbital velocity is the measured velocity of the high velocity maser. The orbital radius can then be found by

$$a = \frac{v^2}{r}, \tag{2.1}$$

where a is the acceleration, v is the orbital velocity, and r is the distance from the central black hole. After the radius has been determined, a distance measurement is made by associating the orbital distance of the red or blue shifted maser feature to the angular distance taken from the VLBI map. The distance becomes

$$D = \frac{r}{\theta}, \tag{2.2}$$

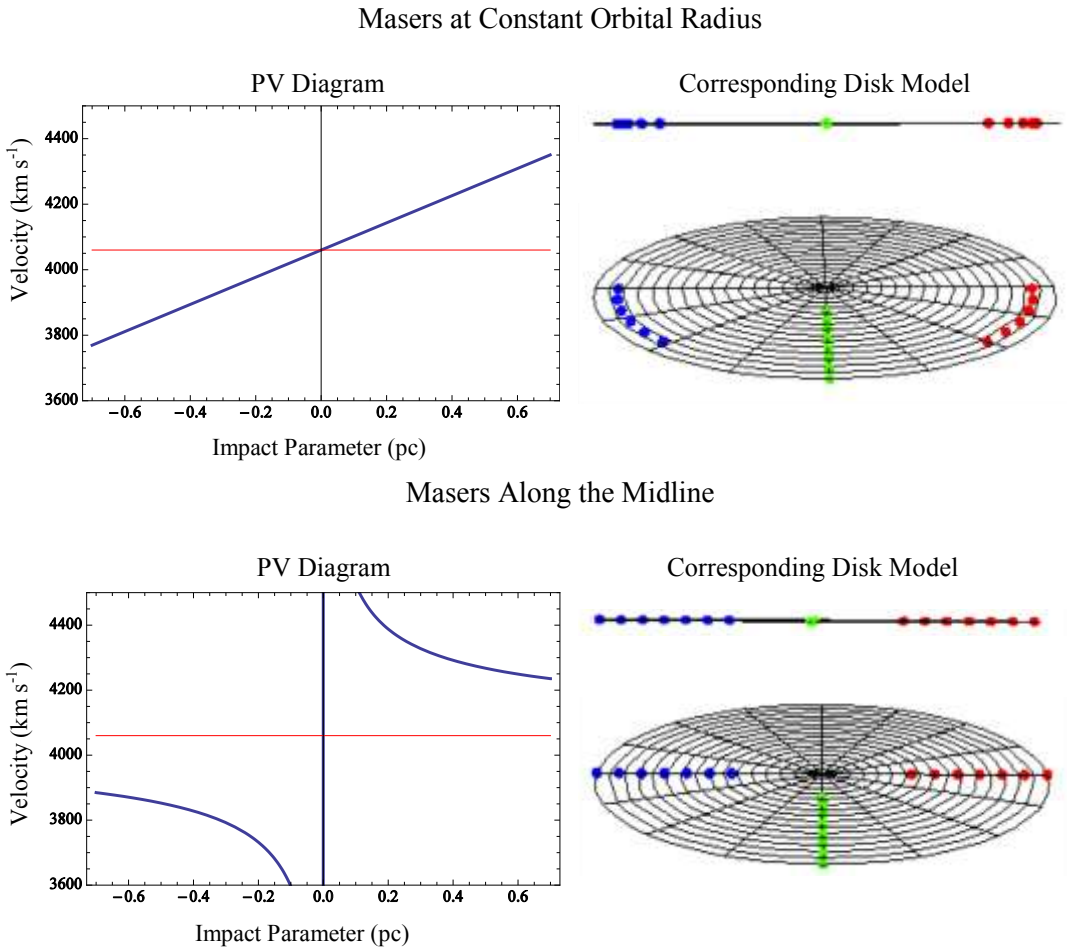

Figure 2.4 This is the theoretical position-velocity (P-V) diagram for masers along the midline and for masers at constant radius. Red and blue dots represent red-shifted and blue-shifted masers. Green dots represent systemic masers. As can be seen, masers found along the midline fit a classic Keplerian curve while masers found at constant radius have a linear change in velocity. The red line represents the systemic velocity of the galaxy.

where θ is the angular distance from the megamaser to the central black hole. The mass of the black hole is easily determined by combining Newton's second law with the gravitational force law. The acceleration is related to the black hole mass and becomes

$$a = \frac{GM_{BH}}{r^2}, \tag{2.3}$$

where G is the gravitational constant and M_{BH} is the central black hole mass.

2.2 Measuring Positions with the Very Long Baseline Array (VLBA)

2.2.1 VLBI Techniques

Radio interferometry is a complex process requiring multiple steps and corrections. In order to use VLBI, two signals must be combined together while making corrections for the phase, delay, clock errors, etc. If they are combined without the proper corrections the source will not be detectable. This subsection will address each of the important correction steps in minimal detail.

When observing a radio source, different baselines will measure a different amplitude for the source. Amplitude calibration fixes the discrepancy. In order to measure the correct intensity two important steps must be taken. First, corrections must be made due to the digital sampler bias and then continuum amplitude calibration must be done. The sampler correction fixes errors due to sampling bias in the correlator when the data is read through its tape feeds and digitized. The continuum amplitude calibration corrects for differences in the amplitude due to weather, gains, and the system temperatures at each antenna.

A critical part of the radio reduction process is getting correct values for the delay and rate of the signal as it enters each of the antennas. The delay is the time difference in the signal between two antennas in a baseline and the rate is the rate at which that delay changes. The delay will

often be represented as a distance because the main source of delay comes from the fact that the antennas are different distances from the source, causing the signal to reach them at different times. See Fig. 2.5 for a representation of many of the sources of delay. Errors in the delay are corrected for while the data is being read into the correlator or afterwards, during the reduction process. As is shown in the figure the delay due to the fact that the antennas are different distances from the target source (also known as geometric delay) is corrected for by taking the scalar product of $\vec{b}$, the vector pointing across the baseline, and $\hat{S}$, the vector pointing away from the antenna towards the source. The delay time can then be measured as

$$\tau_s = \frac{\vec{b} \cdot \hat{S}}{c}, \tag{2.4}$$

where τ_s is the geometric delay and c is the speed of light. This delay is corrected for in the correlator, where the data is read together before the reduction process.

Many of the other sources of delay are corrected for after the data is run through the correlator, during reduction. One of these is the single-band delay, which is delay that is caused by the passage of the signal through the electronics. The reason this is called single-band delay is because it is the same for all frequency bands. Another source that must be corrected for is multi-band delay which is caused from many sources including position error of target source, the antenna position error, the tropospheric delay errors, and the clock error. It is called multi-band delay because the delay changes from one intermediate frequency (IF) band to another. The delay must be known with high accuracy or you will not be able to see your target source.

The troposphere is relatively stable throughout one observing run but may change from observation to observation. For this reason, a set quasars are observed before and after each data set to solve for the tropospheric solution across the sky. This data set is called a geodetic dataset. After the tropospheric solution for each time period is found it is then extrapolated across the entire observing run. The solutions, which were derived from calibrator sources, are then applied to the main source and the correction is complete. In addition to the troposphere, when you observe

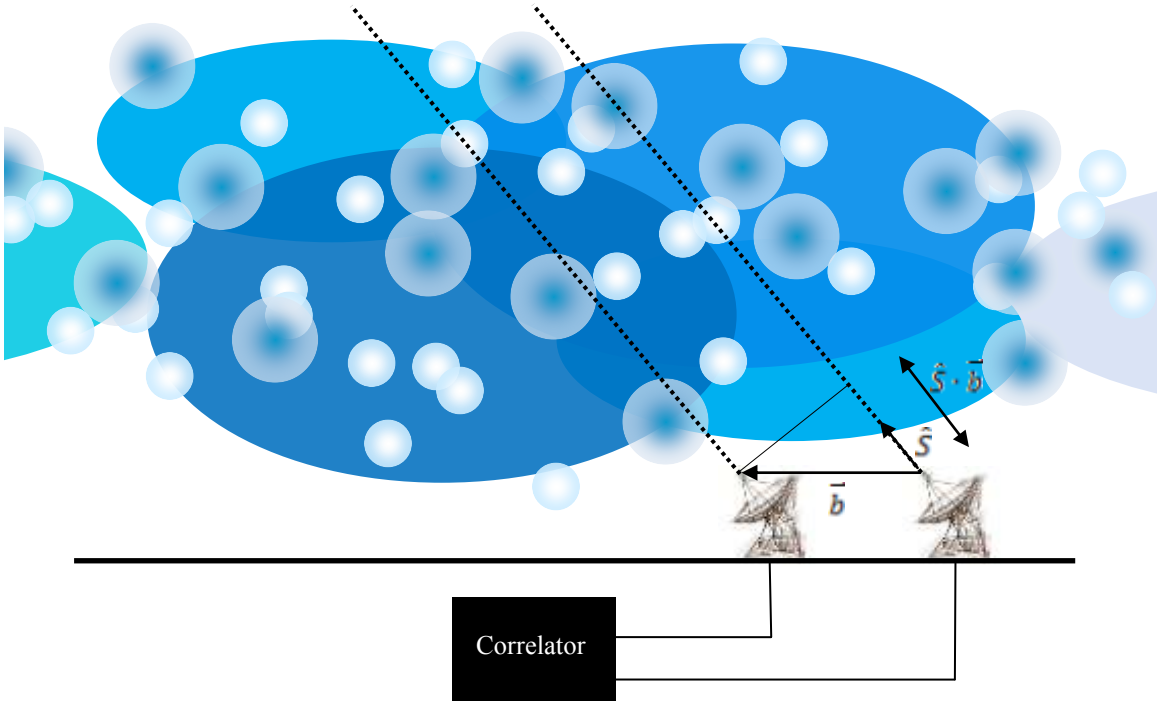

Figure 2.5 A variation of an illustration of some of the sources of delay including geometric delay and delay due to irregularities in water vapor found in the troposphere by (Thompson et al. 2001). As is shown, the geometric delay can be determined by taking the scalar projection of the baseline vector onto the unit vector pointing from the antenna to the source.

a source from multiple locations and at different times, the changes in the ionosphere will effect the delay measured in a given baseline. These changes occur because the ionosphere is stable for only short periods of time. NASA takes accurate records of the ionosphere and we can use those records to make corrections in each baseline. Atomic clocks are used to measure the delay and rate allowing us to correct for the errors. After reduction typical delay error will be less than ten centimeters.

An additional correction that must be accounted for is the error in the parallactic angle of each antenna. This is caused by the rotating orientation of the antenna feeds with respect to the observed source. This can be easily accounted for using packages created for the array.

Bandpass Calibration is necessary because the response of your telescope is not constant across a given IF band. Bandpass calibration is done by observing a bandpass calibrator which is then used to normalize the band response and "flatten" the signal at each frequency. This is important if you want to measure the correct relative amplitudes for each channel in your data cube.

As the earth rotates the velocities of each antenna with respect to the observed source changes. This causes a slight doppler shift that changes with respect to time throughout the observation. This small shift in the frequency must be taken into account if you want to combine datasets from different epochs.

Finally, one of the most important corrections to be made is making sure the phase of your source matches up for each antenna. There are two techniques that can be employed for phase calibration, each having their own advantages and disadvantages. One is called phase referencing and the other is called self calibration. For phase referencing a phase reference, usually a bright quasar near the source whose phase is know extremely well, is observed periodically throughout the observation. The phase solutions are then found by interpolating for periods of time when the source was observed. The major advantage of using phase referencing is that the absolute source position is then known very well because it is then based off of the position of your phase

reference. The other method, self calibration, is done by using a priori information about a bright spectral feature in your source as the phase reference. You can then track the phase of this spectral feature and apply it to the rest of the spectral channels. The disadvantage is that all absolute source position information is lost, only relative position information remains. The major advantage is that no integration time is wasted on a phase reference. This method is used primarily when there is a strong spectral feature and when absolute source positions aren't necessary.

2.2.2 Observations

Our VLBI observations of Mrk 1210 were done with the Very Long Baseline Array (VLBA), which is a set of ten, 30 m radio antennas spread across the United States. The longest baseline runs from Mauna Kea, HI to St. Croix in the U.S. Virgin Islands and is approximately 3000 km. With resolution of over ten times that of the Hubble Space Telescope, this enables us to look deep into the center of the galaxy to study the orbital dynamics of the inner most parsec of its central black hole. These VLBI observations were done at three separate epochs using all the VLBA antennas under the project BK0163. These were done with the K-band receiver. Each observing run consists of two different data set types. These are the geodetic set and the maser set. Geodetic datasets are the result of observing 12-15 quasars at the beginning and end of each observing run. Their purpose is to measure tropospheric and clock delay residuals for each antenna. These results are then applied to the maser set as described in subsection 2.2.3. The date and integration time of each of the three observations can be found in table 2.1. Due to bad system temperatures (See table 2.2) on many of the antennae, the phase was not trackable throughout the observing run in September and the observation was not used in the imaging process. We reduced each VLBI dataset individually using the NRAO Astronomical Image Processing System (AIPS) and then concatenated the data, thus increasing the signal-to-noise ratio. The full reduction process is explained in subsection 2.2.3.

Table 2.1. VLBA Observations

Data Set	Date	Integration hr:m:s
BK0163A	2010-05-22	10:00:00
BK0163B	2010-09-06	09:56:40
BK0163C	2010-07-06	07:40:00

Table 2.2. VLBA Approximate System Temperatures (K)

Antenna	BK163A	BK163B	BK163C
BR	40	100	80
FD	85	70	100
HN	105	90	140
KP	55	100	70
LA	60	70	60
MK	30	40	35
NL	110	140	150
OV	50	55	65
PT	50	60	55
SC	120	130	130

The maser data set was observed using four intermediate frequencies (IFs) with each band containing left circularly polarized (LCP) and right circularly polarized (RCP) radiation. The four IFs were centered at the optical local standard of rest (LSR) velocities of 4270, 4046, 3770, and 3150 km s^{-1}. Each IF covered the systemic, red-shifted, and blue-shifted maser features, with a fourth IF placed outside the maser frequency range. See Fig. 3.1. for the full spectra of Mrk 1210 with the associated velocities.

The target source Mrk 1210 was observed in 40 minute blocks followed by a 2.5 minute observation of the source J0750+1231. Observations of J0750+1231 were done to monitor the changes in delay throughout the observing run. The source 4C39.25 was also periodically observed and was used during the bandpass calibration process.

2.2.3 Calibration

Calibration of VLBI can be an extremely complicated process including many steps and sub-steps. This subsection attempts to summarize the AIPS reduction process used by the MCP, as written and organized through private communication with Dr. Cheng-Yu Kuo. This section presents it in a way that is understandable to the average reader. For a more complete overview of the reduction process, please contact the author or access the NRAO AIPS Cookbook online.

AIPS is a software package for calibration, data analysis, image display, plotting, and a variety of other tasks on radio wavelength astronomical data. It was developed by the National Radio Astronomy Observatory. It contains many packages and sub routines called tasks, verbs, and adverbs. These have been designed for a variety of instruments and arrays, including the VLBA. When running AIPS, the raw data is never changed. Instead, solutions to the various reduction processes are found and stored in SN table and are later applied to the data and converted into CL tables. After all reduction is complete, all finalized CL tables are applied to the data and the image cubes are created. See Table 2.3 for a list of the table types which are critical in the

Table 2.3. Important AIPS Tables for Data Reduction

Table Type	Description
SN	The SN tables are "Solution" tables. The contain solutions that can later be applied to the data set.
CL	The CL tables are "Calibration" tables. They contain the corrections after other tables, like the SN, have been applied.
BP	The BP table is the "Bandpass" table. It contains the information obtained after bandpass calibration.
TY	The TY table is a the "system temperature" table. The system temperature as a function of time for each antennae is contained here.
AN	The AN table is the "Antenna" table. It contains general information about each antenna used during the observation.
FG	The FG tables are "Flag" tables. They contain flags that have been applied by the user for the observation.
PL	The PL tables are "Plot" tables. They contain plots that have been created by the user and can later be exported.
GC	The GC tables are the "Gain" tables. They contain information about the gain of each baseline.
WX	The WX tables are the "Weather" tables. They contain information about the weather at each of your antennas.

Note. — The different table types used during the reduction process in AIPS.

data reduction process. See also Fig. 2.6 for the reduction process we used in AIPS. For a more complete explanation of AIPS and its many functions, consult the AIPS Cookbook.

Before calibrating the maser data set. the geodetic set must be reduced and the troposphere delay and clock error solution must be found. For the three datasets, a total of 23 separate quasars were observed. The geodetic sets were reduced using a general AIPS reduction. We then measured the multi-band delay using the task 'MBDLY'. The tropospheric delay and clock error was then derived using the task 'DELZN'. These solutions were later applied to the maser data set.

For the maser data set, we first corrected for ionospheric effects and errors in the earth orientation parameters by running 'VLBATECR' and 'VLBAEOPS'. Following that process the amplitude was calibrated by first using the task 'ACCOR' which corrects for biases due to the sampling error in the correlator. This was followed by amplitude calibration across the continuum using the task 'APCAL'. We then corrected for the parallactic angle correction using the task 'CLCOR'. The rates and clock errors that were obtained during the reduction of the geodetic set were then

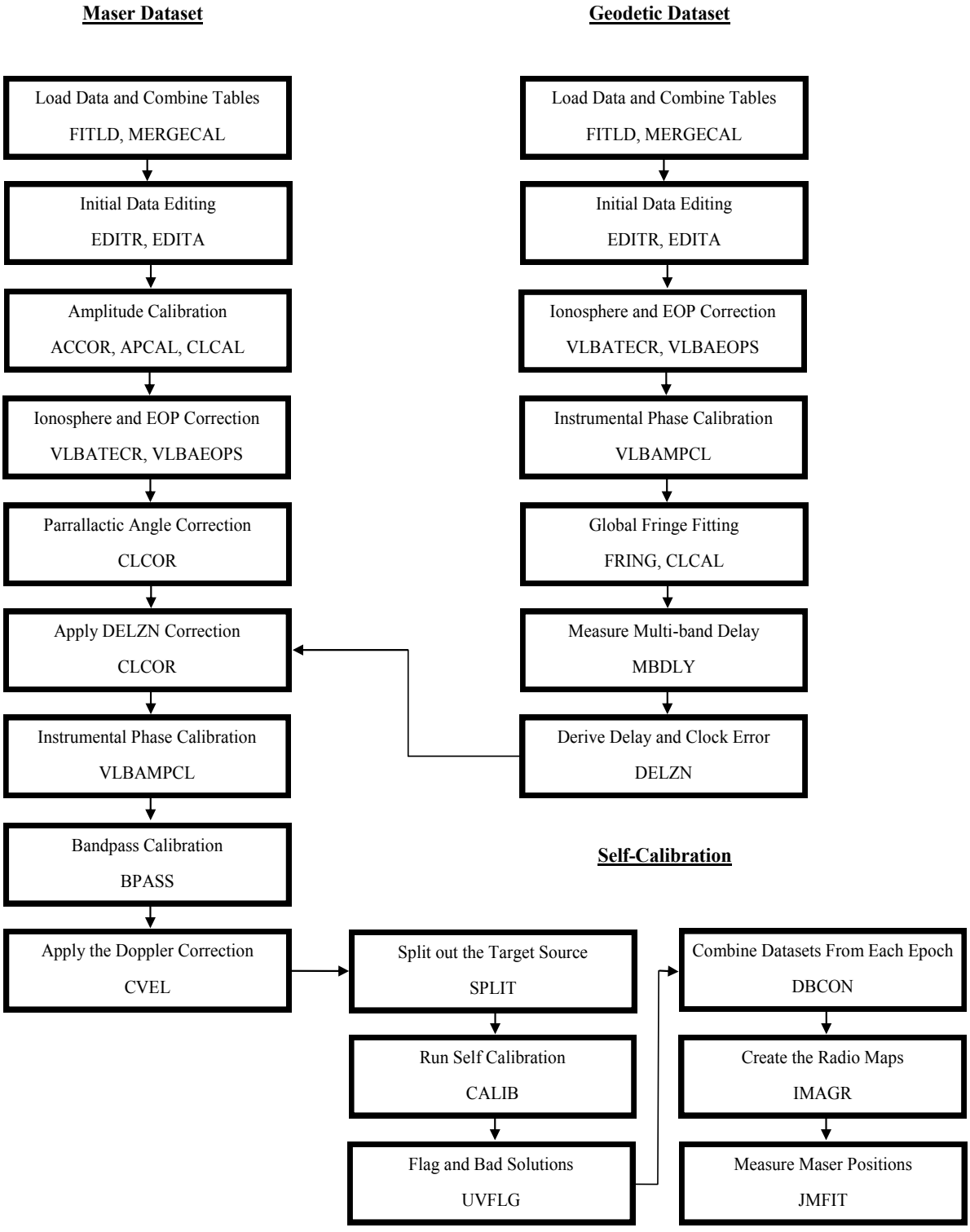

Figure 2.6 This flowchart outlines each reduction process for theVLBA in AIPS and states the task or verb used in each reduction step.

applied to the dataset. We then corrected for the single band and multi band delay using the verb 'VLBAMPCL' followed by the task "FRING'. This was followed by bandpass calibration using 'BPASS'. We then corrected for Doppler effects due to the rotation of the earth using the task 'CVEL' and split the target source in preparation for self-calibration.

Self-calibration was done using the task 'CALIB' and was based on a priori information obtained from GBT observations. GBT observations show a strong maser feature centered at a velocity of 4228 km s^{-1}. Because we know masers are detected as point sources, this feature was used to measure and correct for variations in the phase throughout the observation. After correcting for the variations in the phase and doing minor editing of the data, we then combined the datasets using the task 'DBCON' in preparation for imaging.

Imaging was done using the task 'IMAGR'. The images were 256×256 pixels with 0.00005 asec $pixel^{-1}$. Natural weighting, which applies weights to each antenna based on their system temperatures, was used during this process. Each channel map showed rms values of about 1.71 mJy. The maps were cleaned down to a cutoff of three times the rms noise level, which is approximately 5.13 mJy. The cleaning algorithm improves the quality of each channel map by finding the brightest emission in the map and subtracting off the telescopes response to a point source (the beam) and marking its position on the finalized map. This process is often called deconvolution. The cleaning was done until a cutoff of three times the noise level to ensure that all marked positions in the final map are real maser detections and not the result of high noise in some of the channels. For a more detailed explanation of the cleaning process see (Gary Accessed February 23, 2012).

Figure 2.7 This is the Robert C. Byrd Green Bank Telescope (GBT). With its enormous 100-meter diameter dish, the GBT is the largest fully steerable telescope in the world. Photograph provided by the author.

2.3 Measuring Accelerations with the Green Bank Telescope (GBT)

The Robert C. Byrd Green Bank Telescope (GBT), is the world's premiere single-dish radio telescope operating at meter to millimeter wavelengths. Its enormous 100-meter diameter collecting area, its unblocked aperture, and its excellent surface accuracy provide unprecedented sensitivity across the telescope's full 0.1 - 116 GHz operating range, a larger frequency range than any other telescope. The GBT is fully steerable, and 85% of the entire celestial sphere is accessible (NRAO Accessed February 21, 2012). See Fig. 2.7. With unparalleled capabilities, the GBT was an ideal instrument for our observations of Mrk 1210.

Table 2.4. GBT Observations

Date	Integration (hr:m:s)	Band Width (MHz)	Tsys (K)
2004-04-08	00:51:26.3	200	44.66
2004-08-29	00:29:23.6	200	82.09
2004-11-14	00:13:58.2	200	26.40
2006-10-24	00:09:06.8	200	55.28
2008-11-11	00:45:28.3	200	32.05
2010-01-10	00:18:13.1	200	30.60
2010-02-25	00:18:11.4	200	33.22
2011-06-03	00:36:26.9	200	50.34

Under the proposals submitted and telescope time obtained by Dr. James A. Braatz, Dr. James Condon, and Violetta Impellizzeri in the NRAO, the GBT took a total of ten spectral observations of Mrk 1210 from April 2004 through June 2011. Observations were done with the 18-22 GHz K-band receiver using a total power nodding mode. The observations were done with two separate spectral windows, which gave a total bandwidth of 380 MHz. Further details of these observations can be found in Table 2.4. Residuals were obtained in IDL (Interactive Data Language) using the GBTIDL package created by the NRAO.

Chapter 3

Results and Discussion

3.1 Unique Spectral Profile

The spectral profile of Mrk 1210 is not entirely characteristic of classic water megamaser disks. As shown in Fig. 3.1, the spectra has highly red-shifted and blue-shifted features, which suggests the features may come from a disk. In addition, the spectra shows another strong red-shifted feature, not equally spaced from the recession velocity. Classic disks do not contain this type of structure. The systemic maser feature is barely detectable with the GBT. Due to its low intensity and lack of detectability in subsequent observations, the accelerations of this feature were not measured. For this reason Mrk 1210 cannot be used for cosmology.

With a lack of systemic features, a direct distance measurement cannot be made. However, using the Hubble constant obtained from (Freedman et al. 2001), an approximate distance to Mrk 1210 was obtained and a black hole mass measurement was calculated.

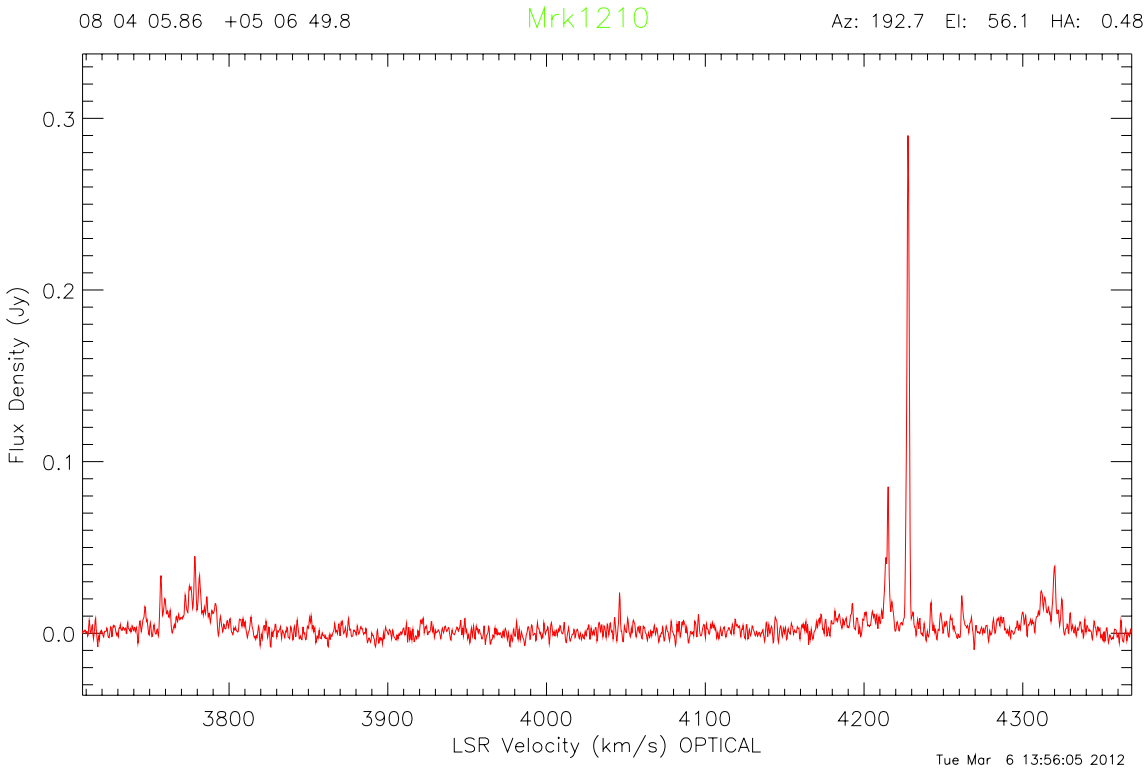

Figure 3.1 This is the spectral profile of Mrk 1210 as taken by the GBT. The spectra show the classic triple peaked profile which is typical in megamaser accretion disks. The spectra shows a weak feature at the systemic velocity and two features equally spaced in velocity on each side. There is also an extremely bright feature found between the systemic feature and the high velocity red-shifted feature. This is not typical in traditional H_2O megamaser disks.

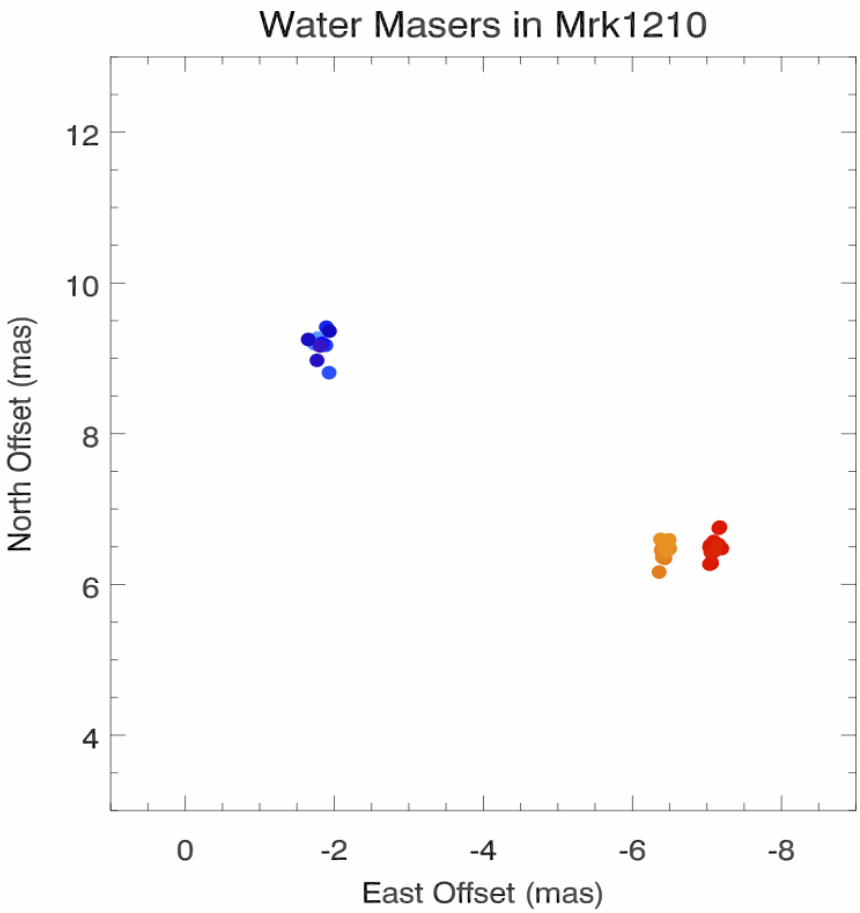

Figure 3.2 A VLBI map of the megamasers in Mrk 1210 taken by the VLBA. The spots are colored according to line-of-sight velocity, with red signifying red-shifted velocities and blue signifying blue-shifted velocities. If the features are in a disk, they do not follow a Keplerian velocity curve with higher velocities toward the center of the disk.

3.2 Maser Positions

Maser position measurements were measured in AIPS using the task 'JMFIT'. This task fits a 2-dimensional Gaussian to each of the maser features on the maps. The positions were measured and plotted with blue signifying blue-shifted masers and red signifying the red-shifted masers as shown in Fig. 3.2.

As can be seen in the radio map, the orange maser feature that is closer to the center of the supposed disk structure has a lower velocity than its red counterpart. This is not typical of other disk structures as explained in section 2.1. Kepler's laws would indicate that higher velocities should be found near the center of the disk if the masers lie along the midline. This may be evidence that the maser features are part of an outflow or that the maser features are part of a tilted disk, with the orange maser feature located away from the midline. See section 3.4 for additional evidence that the masers are indeed in a disk.

3.3 Accelerations of Megamasers

As mentioned previously, the GBT spectra were used to measure the accelerations of each individual maser. The velocities of the maser features with their corresponding errors were determined by fitting a Gaussian profile to each feature. The velocities with their associated MJD are shown in Fig. 3.3. Specific maser features were then tracked through each observation and the acceleration and error were measured by fitting a line through each of these points. A weight of $1/\sigma^2$ was placed on each velocity point for fitting, where σ is the measured error on each. The measured velocities and accelerations with their associated errors are given in Table 3.1. A plot of these values is shown in Fig. 3.4.

The measured accelerations of Mrk 1210 also provide evidence that the masers are in a disk. As is shown in Tab. 3.1 our measured accelerations give information on the line-of-sight motion of

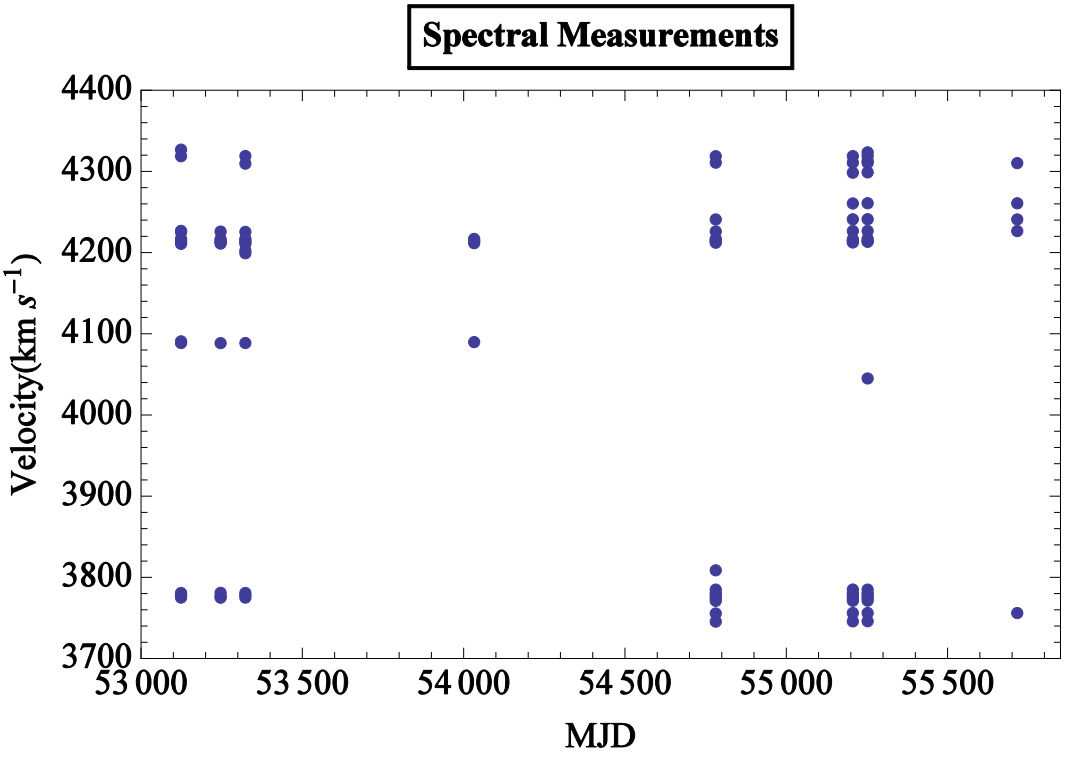

Figure 3.3 This shows the velocities of Mrk 1210 with their associated MJD. These were found by fitting a gaussian to the spectral profile of each maser feature. As can be seen, there are large amounts of time between many of the observations. This introduced large errors into the acceleration measurements as shown in Table 3.1.

Table 3.1. Velocity and Acceleration Measurements

Velocity (km s^{-1})	δV	Acceleration (km s^{-1} yr^{-1})	δA
3746.80	0.07	0.245	0.105
3757.13	0.11	-0.035	0.005
3772.27	0.03	0.117	0.091
3776.06	0.02	-0.071	0.206
3775.54	0.06	0.190	0.177
3778.42	0.05	0.228	0.035
3781.88	0.08	0.221	0.423
3781.39	0.05	0.040	0.005
3786.00	0.06	0.066	0.046
4089.65	0.11	-0.130	0.157
4212.05	0.04	0.148	0.496
4213.70	0.03	0.478	0.497
4213.92	0.02	-0.224	0.184
4214.88	0.05	0.248	0.038
4215.93	0.05	0.231	0.028
4227.52	0.03	0.234	0.105
4242.06	0.02	0.206	0.040
4261.74	0.05	0.126	0.159
4319.84	0.07	0.112	0.016

Note. — These are the velocities and accelerations with their associated errors.

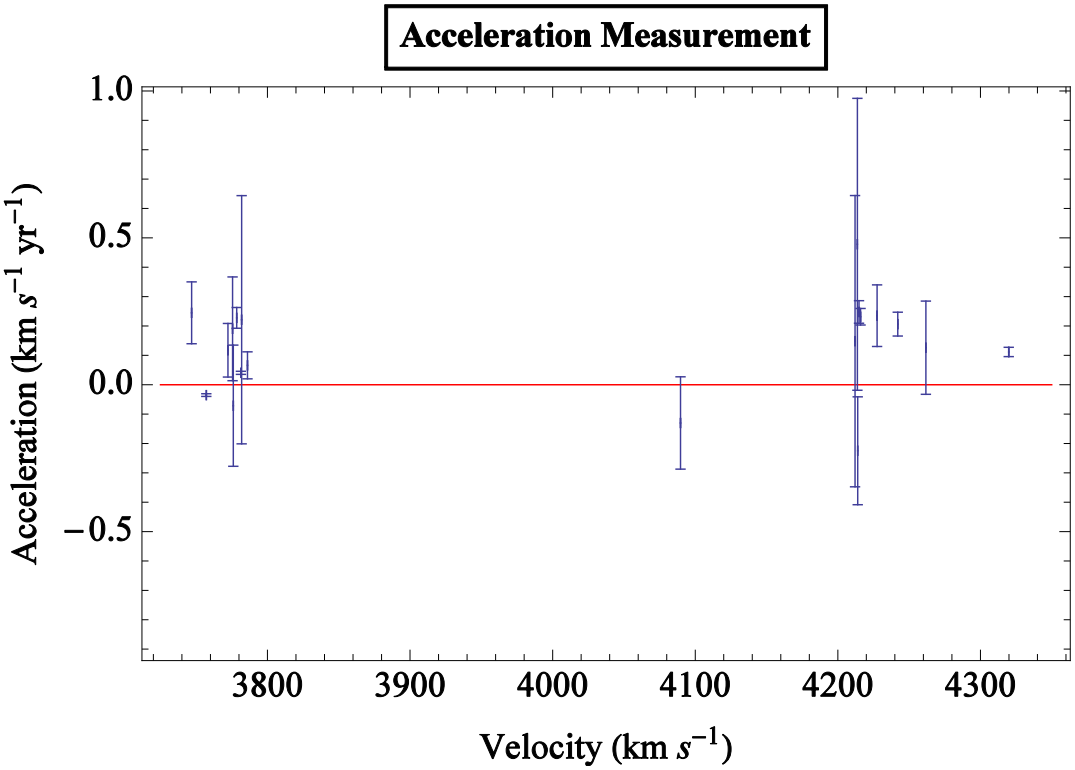

Figure 3.4 This shows the acceleration measurement of Mrk 1210 plotted vs velocity. As is shown, the majority of the accelerations are zero indicating that these masers fall along the midline of the disk. The masers corresponding to the orange maser features have slightly positive accelerations, implying that they me be off the midline on the front side of the accretion disk.

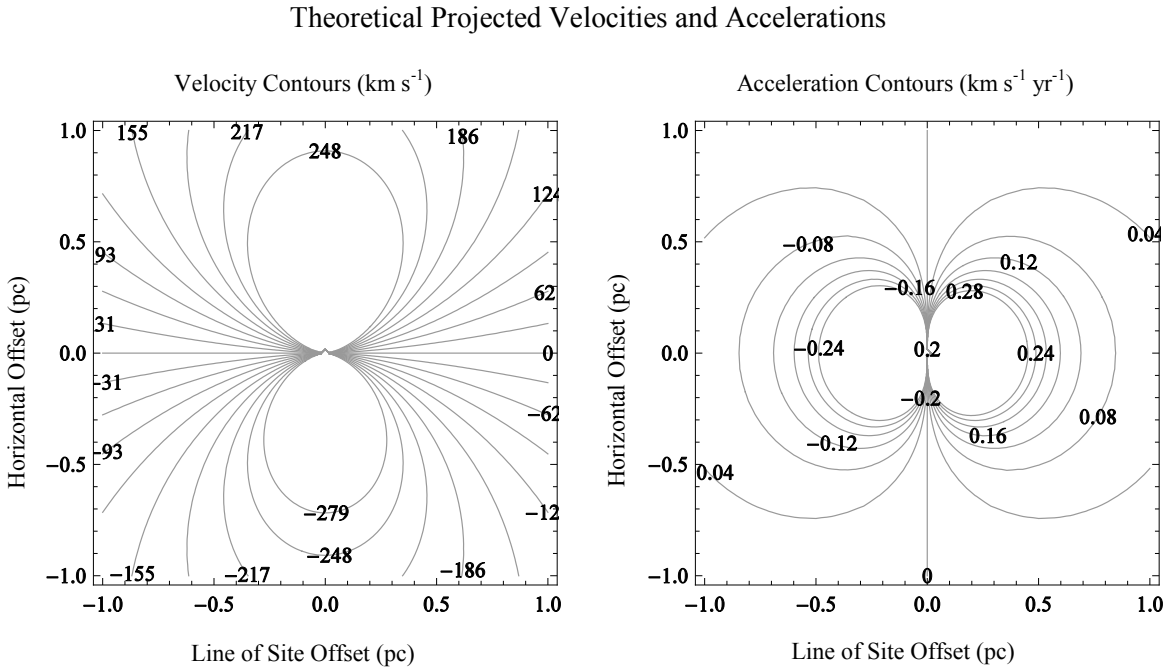

Figure 3.5 Velocity and acceleration contours in a flat maser disk as seen by an observer looking from the right of the figure, assuming a black hole mass of 1.3×10^7 $M_\odot$ and a tilt of 8.7 degrees. As can be seen, highest velocities are found on the midline closest to the central black hole and zero accelerations are found on the midline with positive accelerations on the front side of the disk and negative accelerations on the back.

masers. See Fig. 3.5 for a theoretical contours of the velocities and accelerations that should be observed from different parts of the disk. As is shown in the model, we expect positive accelerations from maser clouds on the front side of the disk, and nearly zero acceleration from masers coming from the disk "midline". Our measured GBT accelerations of the high recession velocity masers are all near zero, with a slight positive acceleration on the orange maser spot. This is consistent with these masers arising near the midline of an edge-on disk with the third maser on the front side of the disk.

3.4 External Megamaser Disk Evidence

The orientation of the maser features in the VLBI map in combination with the features shown in the GBT spectra may suggest that the maser spots are located in the accretion disk of the AGN with some inclination angle θ. Additional evidence that the masers lie in a nearly edge-on disk is shown in Fig. 3.6 (Middelburg et al. 2004). The configuration of the disk is nearly perpendicular to the continuum emission and suggests that it may be due to some outflow from the disk. Since the red and blue maser features have almost an equal difference in velocity from the recession velocity of the galaxy, we will make the assumption that they are an equal distance from the AGN along the midline of the disk. This assumption is somewhat valid because this is what we see in many other H_2O megamaser disks.

Since the disk has some inclination angle, we are not observing the true velocities of the masers, only a projection of the true rotation velocity. For this reason, we cannot use the velocities that we measure to calculate the mass of the central black hole. We must first solve for the inclination angle θ, by using the third group of orange maser spots, which appears to be offset from the midline of the disk.

Each of the velocities we measure are scaled by $\cos\theta$. For this reason we can use the velocities of the highly blue-shifted and red-shifted masers to estimate what projected velocities and accelerations we are expected to see from any position on the disk. From this model, we can determine the location of third maser spot on the disk and find the inclination angle of the disk and eventually the true mass of the central black hole.

3.5 Our Disk Model for Mrk 1210

The Position-Velocity (P-V) diagram for the disk is shown in Fig. 3.7. If the masers were to all lie along the midline of the disk, the P-V diagram would follow a pattern depicted theoretically by the

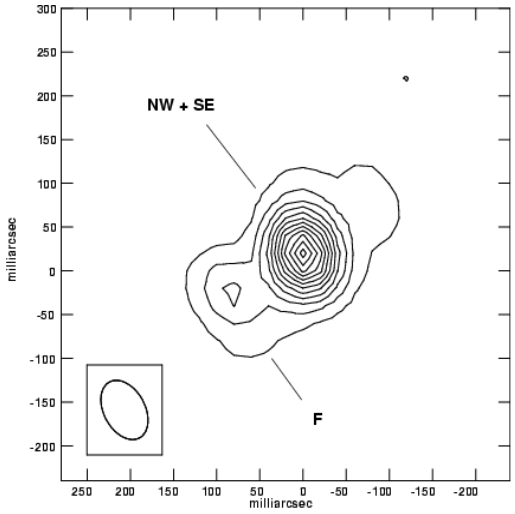

(a) MERLIN 6 cm image of Mrk 1210. Offsets are relative to RA 08:04:05.86011, Dec 05:06:49.8992 (J2000), peak flux density is 24.1 mJy/beam, contours are 1 mJy/beam× (−1 , 1, 3, 5, 7, . . . , 23), beam size is 72.7 mas × 47.6 mas and uniform weighting was used.

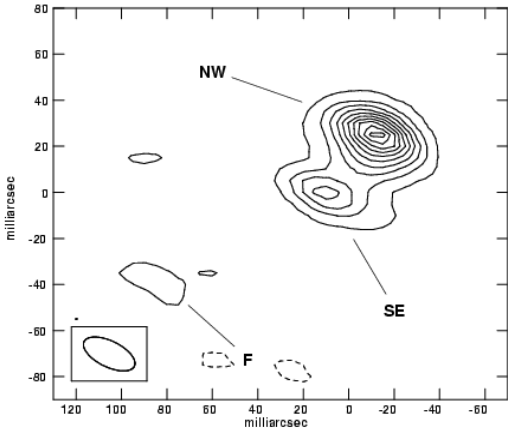

(b) EVN 18 cm image of Mrk 1210. Offsets are relative to RA 08:04:05.856, Dec 05:06:49.83 (J2000), peak flux density is 19.8 mJy/beam, contours are 1 mJy/beam× (−1 , 1, 3, 5, . . . , 19), beam size is 24.6 mas × 11.3 mas and uniform weighting was used.

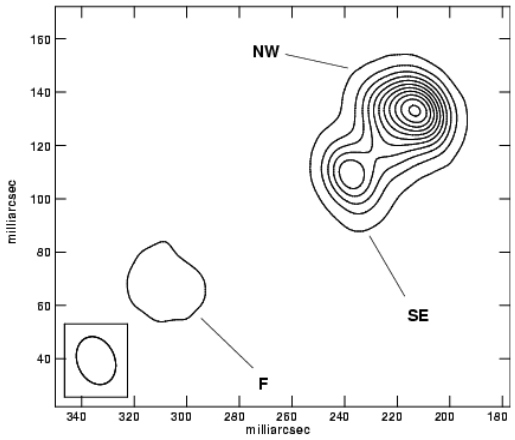

(c) VLBA 18 cm image of (Obj)Mrk 1210(Obj). Offsets are relative to RA 08:04:05.841, Dec 05:06:49.72 (J2000), peak flux density is 21.6 mJy/beam, contours are 1 mJy/beam× (−1 , 1, 3, 5, . . . , 21), beam size is 18.6 mas × 14.2 mas and natural weighting was used.

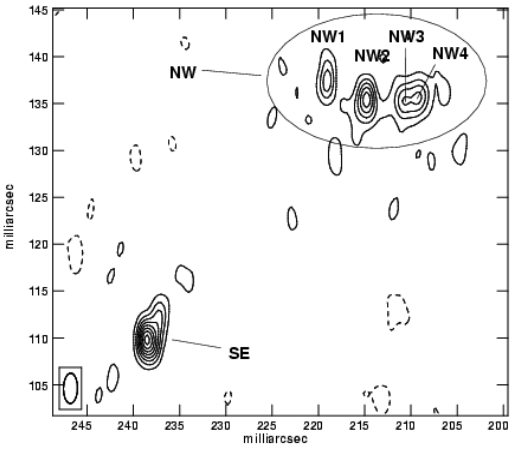

(d) VLBA 6 cm image of (Obj)Mrk 1210(Obj). Offsets are relative to RA 08:04:05.841, Dec 05:06:49.72 (J2000), peak flux density is 2.5 mJy/beam, contours are 0.1 mJy/beam× (−3 , 3, 6, . . . , 24), beam size is 3.2 mas × 1.5 mas and uniform weighting was used.

Figure 3.6 This is the radio map of Mrk 1210 taken from (Middelburg et al. 2004). Our map of the central disk of Mrk 1210 is small compared to the rest of the map. By comparing this with Fig. 3.2, it can be seen that the emission is perpendicular to the line of masers. This is evidence that the masers are found within a disk, with the continuum emission being associated with outflow from the central black hole.

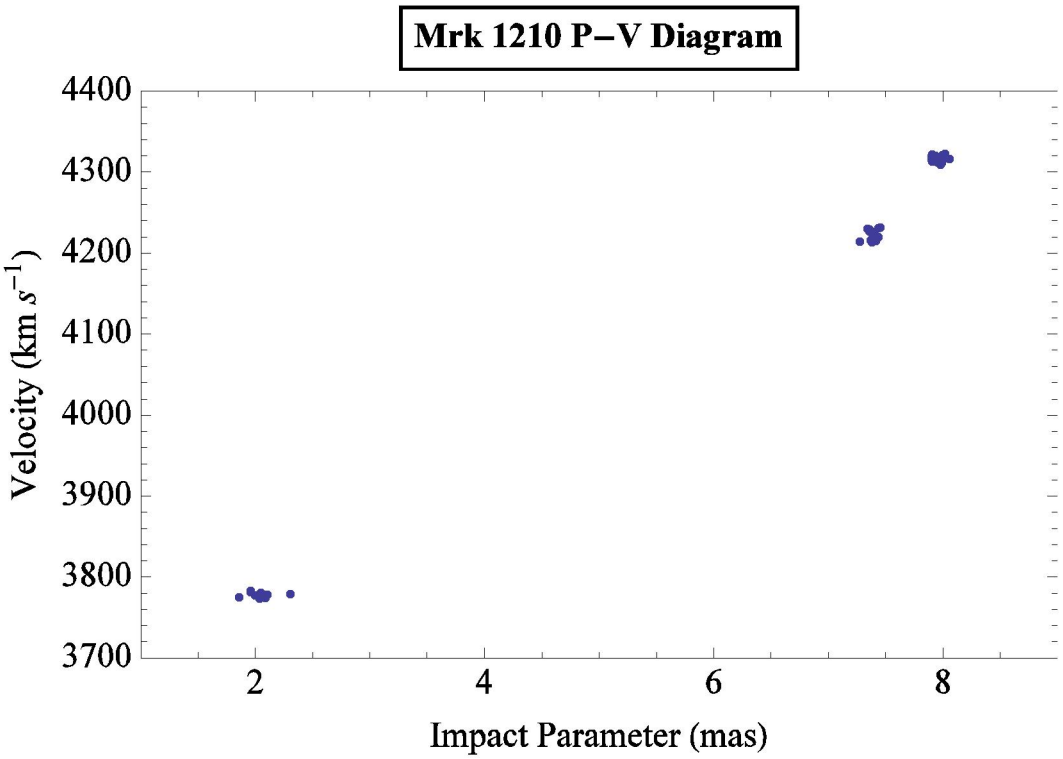

Figure 3.7 This is the Position-Velocity (P-V) of Mrk 1210. As can be seen, the velocities are fit by a linear trend, indicating that the masers may be found close to the same radius in the accretion disk.

equation

$$v = \pm\sqrt{\frac{GM}{r}}, \tag{3.1}$$

as can be shown by Kepler's laws. By observing the P-V diagram it can be seen that a linear fit would be more appropriate. This indicates that all three maser spots may lie near the same radius from the black hole in a tilted disk.

We calculated a distance 55.3 Mpc to Mrk 1210 by using Hubble's law with a value for H_0 of 73 km s^{-1} Mpc^{-1} as shown in (Freedman et al. 2001). Using this distance measurement, the linear distance from the blue and red shifted masers to the central AGN was determined to be 0.80 pc.

Table 3.2. Maser Positions and Intensities

Velocity (km s^{-1})	Intensity mJy/BEAM	East-Offset (mas)	Error	North-Offset (mas)	Error
4322.4	4.545	-7.061	0.051	6.291	0.144
4321.6	4.841	-7.174	0.081	6.760	0.161
4320.7	1.567	-7.157	0.015	6.529	0.038
4319.8	1.268	-7.087	0.024	6.536	0.053
4319.0	4.423	-7.044	0.087	6.518	0.125
4318.1	5.029	-7.036	0.054	6.268	0.113
4317.2	4.282	-7.062	0.063	6.279	0.119
4316.3	3.740	-7.199	0.066	6.476	0.216
4315.5	3.894	-7.160	0.054	6.745	0.170
4314.6	7.773	-7.082	0.033	6.522	0.077
4313.7	5.350	-7.094	0.065	6.571	0.141
4312.9	6.097	-7.036	0.060	6.495	0.102
4312.0	12.15	-7.054	0.025	6.426	0.048
4311.1	7.239	-7.102	0.068	6.443	0.129
4310.3	3.623	-7.068	0.093	6.422	0.160
4309.4	6.006	-7.123	0.041	6.504	0.104
4231.4	5.104	-6.359	0.077	6.164	0.120
4230.5	3.739	-6.436	0.064	6.346	0.104
4229.7	56.17	-6.390	0.006	6.462	0.013
4228.8	127.4	-6.400	0.003	6.448	0.006
4227.9	101.6	-6.400	0.003	6.455	0.007
4227.1	46.68	-6.396	0.007	6.442	0.014
4226.2	7.902	-6.403	0.040	6.360	0.094
4219.3	3.461	-6.500	0.122	6.475	0.247
4217.5	7.517	-6.450	0.045	6.442	0.086
4216.7	11.01	-6.493	0.030	6.592	0.066
4215.8	24.62	-6.432	0.016	6.483	0.025
4214.9	15.98	-6.458	0.018	6.440	0.045
4214.1	11.80	-6.379	0.023	6.598	0.054
4213.2	6.721	-6.456	0.047	6.506	0.079

Table 3.2 (cont'd)

Velocity (km s^{-1})	Intensity mJy/BEAM	East-Offset (mas)	Error	North-Offset (mas)	Error
3782.5	6.577	-1.776	0.040	9.267	0.117
3781.6	11.09	-1.736	0.028	9.193	0.068
3780.8	5.057	-1.837	0.060	9.191	0.110
3779.0	5.651	-1.931	0.072	8.810	0.114
3778.2	8.401	-1.887	0.038	9.173	0.080
3777.3	3.706	-1.894	0.141	9.413	0.153
3776.4	8.534	-1.836	0.043	9.200	0.076
3775.6	6.221	-1.935	0.060	9.361	0.118
3774.7	4.504	-1.651	0.082	9.250	0.108
3773.8	4.049	-1.769	0.071	8.974	0.135

The detected velocity of the highly blue-shifted and red-shifted masers is roughly $\pm$265 km s^{-1} relative to the galaxy's recession velocity, indicating that they are about the same distance from the central black hole. A complete list of maser positions with associated velocities and accelerations are given in Tab. 3.1 and 3.2. By using the velocities of the highly red and blue shifted maser features, coupled with the known distance of the masers from the AGN, we determined the projected theoretical velocities and accelerations that we should observe for a maser on a given location on the disk. Contour plots of these values are shown in Fig. 3.5.

From the VLBI map in conjunction with the velocity and acceleration contour plots, we determined that the projected distance of the orange maser spots along the midline of the disk is 0.64 pc. Using this distance in combination with the VLBI map, it was determined that the disk has a tilt of $\theta = 8.7^{\circ}$. A model depicting the maser spots and positions can be found in Fig. 3.8. With this information, the true velocity of the highly blue shifted masers can be determined by

$$v = \frac{v_{meas}}{\cos\theta}. \tag{3.2}$$

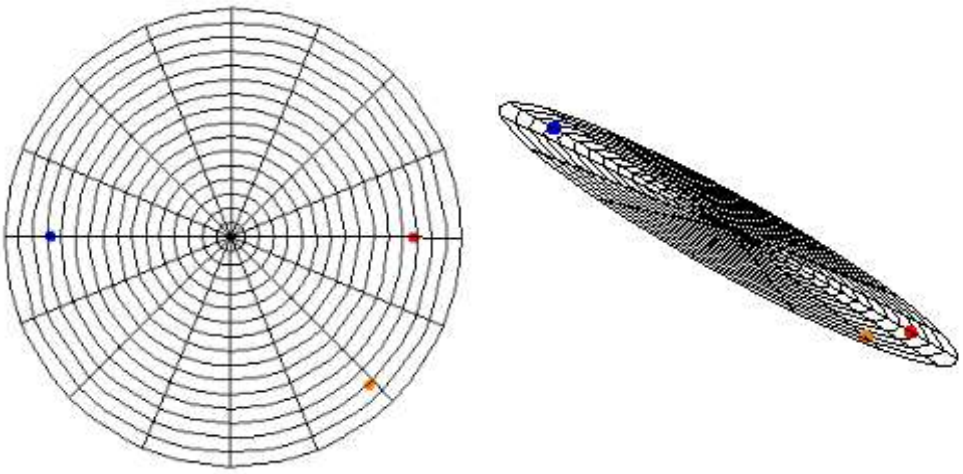

Figure 3.8 This is the proposed disk model of the circumnuclear H_2O megamasers in Mrk 1210. The red and blue spots correspond to the red-shifted and blue-shifted masers. The orange feature has a slightly slower velocity than the red feature. The figure on the left shows a top down view of the disk. The figure on the right shows how the disk fits the maser features shown in the VLBI map (See Fig. 3.2).

Figure 3.9 The measured velocities are the true velocities projected along the line of sight. The true velocities of the masers can be found geometrically after the tilt angle is calculated (see equation 3.2). By finding the true velocities, coupled with their distance from the black hole, we can find the mass of the black hole.

Where θ is the tilt angle of the disk along the midline, with v_{meas} =265km s^{-1}, as mentioned earlier. Using this relation we determined that the true velocity of the highly red and blue shifted masers is approximately 268.8 km s^{-1} (See Fig. 3.9). Using this velocity and equation 3.2, this gives a black hole mass of 1.3×10^7 M$_\odot$.

3.6 The Black Hole Mass and the M-σ Relation

A mass of 1.3×10^7 $M_\odot$ for Mrk 1210 is consistent with other central black hole masses which are typically found to be anywhere from $10^6 - 10^8$ $M_\odot$. The mass is also congruent with our predictions based on the M-σ relation. According to (Gu et al. 2006), the stellar bulge velocity dispersion (σ) is 114 km s^{-1}. In (Gultekin et al. 2009), the velocity dispersion is related to the central mass by

$$M_{BH} = 10^{8.12} M_\odot \left(\frac{\sigma}{200 \text{ km s}^{-1}}\right)^{4.24}. \tag{3.3}$$

This would imply a black hole mass of 1.22×10^7 $M_\odot$, which is extremely close to our measurement. Fig. 3.10 shows the M-σ relation determination, based on the calculations of a large number of central black hole masses.

3.7 The Future of the Project

Adding in additional observations of Mrk 1210 would be extremely beneficial. With eight spectral observations taken over a period of seven years many of the observations have large periods of time between them. This caused a large amount of error in our acceleration determination. Over the course of the GBT's observing period, spectral observations of Mrk 1210 were taken by the Effelsburg telescope in Germany. Adding in spectral data from the Effelsburg telescope would put larger constraints on our models providing better accelerations and would give us a more accurate

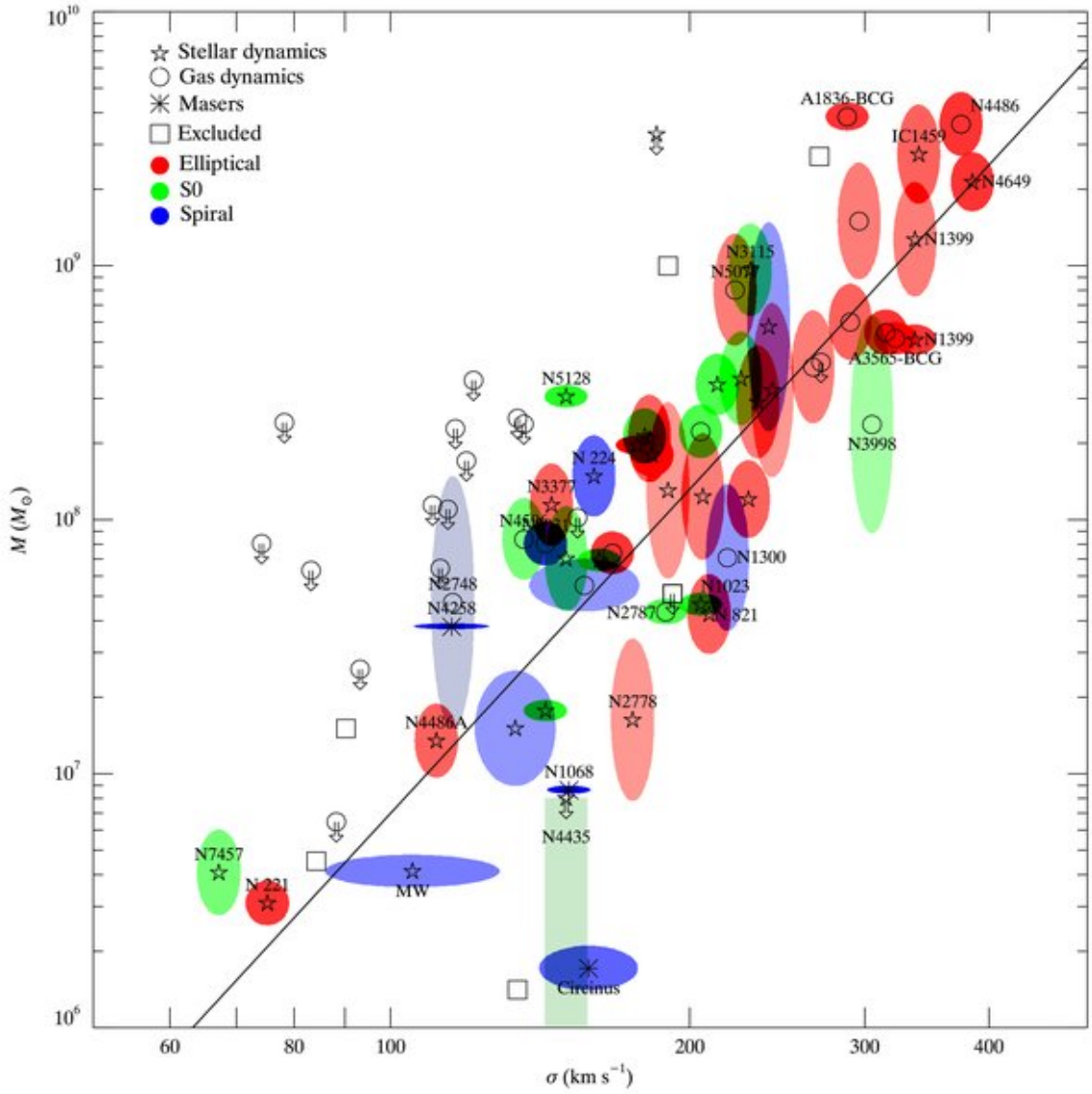

Figure 3.10 M-σ relation for galaxies with dynamical measurements. The symbol indicates the method of BH mass measurement: stellar dynamical (pentagrams), gas dynamical (circles), masers (asterisks). Arrows indicate $3\sigma 68$ upper limits to BH mass. If the $3\sigma 68$ limit is not available, we plot it at three times the $1\sigma 68$ or at 1.5 times the $2\sigma 68$ limits. For clarity, we only plot error boxes for upper limits that are close to or below the best-fit relation. The color of the error ellipse indicates the Hubble type of the host galaxy: elliptical (red), S0 (green), and spiral (blue). The saturation of the colors in the error ellipses or boxes is inversely proportional to the area of the ellipse or box. Squares are galaxies that we do not include in our fit. The line is the best fit relation to the full sample: $M_{BH} = 10^{8.12}\ M_\odot(\sigma/200\text{km s}^{-1})^{4.24}$. The mass uncertainty for NGC 4258 has been plotted much larger than its actual value so that it will show on this plot. For clarity, we omit labels of some galaxies in crowded regions (Gultekin et al. 2009).

mass measurement. With more frequent observations, each maser velocity could be measured with much higher accuracy, ensuring that the acceleration determinations are accurate. With accurate parameters, better constraints could be put on our disk model and give us greater confidence that the proposed disk is real. This object would be interesting to monitor in several years to see if systemic maser features have appeared. Without systemic features Mrk 1210 cannot be used for cosmological purposes. If they were to flare it would make it a much more valuable object overall.

Bibliography

Advameg. Accessed February 29, 2012, http://www.scienceclarified.com/scitech/Lasers/The-Development-of-Lasers.html

Braatz, J. A. Accessed February 2, 2012, https://safe.nrao.edu/wiki/bin/view/Main/MegamaserCosmologyProject

Braatz, J. A., Reid, M. J., Humphreys, E. M. L., Henkel, C., Condon, J. J., & Lo, K. Y. 2010, The Astrophysical Journal, 718, 657

Buizer, J. D. 2007, Proceedings IAU Symposium, 242, 102

CalTech. Accessed February 29, 2012, http://ned.ipac.caltech.edu/level5/March04/Torres/Torres2_4.html

Ferrarese, L., & Merritt, D. 2000, The Astrophysical Journal, 539, L9

Freedman, W. L., et al. 2001, The Astrophysical Journal, 553, 47

Gary, D. E. Accessed February 23, 2012, http://web.njit.edu/~gary/728/Lecture7.html

Gu, Q., Melnick, J., Fernandes, R. C., Kunth, D., Terlevich, E., & Terlevich, R. 2006, Monthly Notices of the Royal Astronomical Society, 366, 480

Gultekin, K., et al. 2009, The American Astronomical Society, 698, 198

Lo, K. Y. 2005, Annual Reviews of Astronomy and Astrophysics, 43, 625

Middelburg, E., et al. 2004, A&A, 417, 925

NRAO. Accessed February 21, 2012, https://science.nrao.edu/facilities/gbt

—. Accessed February 29, 2012, http://www.cv.nrao.edu/course/astr534/Interferometers2.html

—. Accessed March 7, 2012, http://www.nrao.edu/whatisra/hist_reber.shtml

Reid, M. J., Braatz, J. A., Condon, J. J., Greenhill, L. J., Henkel, C., & Lo, K. Y. 2009, The Astrophysical Journal, 695, 287

Ryden, B., & Petersen, B. 2010, Foundations of Astrophysics (Addison-Wesley), 489

Sullivan, W. T. 1978, Sky and Telescope, 101

Thompson, A. R., Moran, J. M., & George W. Swenson, J. 2001, Interferometry and Synthesis in Radio Astronomy, 2nd edn. (Wiley Interscience), 530

Wikipedia. Accessed March 29, 2012, http://en.wikipedia.org/wiki/Active_galactic_nucleus

Wu, Y.-Z., Zhang, E.-P., Liang, Y.-C., Zhang, C.-M., & Zhao, Y.-H. 2011, The Astrophysical Journal, 730, 121